Title
Study of the decay B̄0→Λc+p̄π+π- and its intermediate states

Permalink
https://escholarship.org/uc/item/8qh6x2sq

Journal
Physical Review D, 87(9)

ISSN
2470-0010

Authors
Lees, JP
Poireau, V
Tisserand, V
et al.

Publication Date
2013-05-01

DOI
10.1103/physrevd.87.092004

Peer reviewed

Study of the decay $\bar{B}^0 \to \Lambda_c^+ \bar{p}\pi^+\pi^-$ and its intermediate states

J. P. Lees,[1] V. Poireau,[1] V. Tisserand,[1] E. Grauges,[2] A. Palano,[3a,3b] G. Eigen,[4] B. Stugu,[4] D. N. Brown,[5] L. T. Kerth,[5] Yu. G. Kolomensky,[5] G. Lynch,[5] H. Koch,[6] T. Schroeder,[6] D. J. Asgeirsson,[7] C. Hearty,[7] T. S. Mattison,[7] J. A. McKenna,[7] R. Y. So,[7] A. Khan,[8] V. E. Blinov,[9] A. R. Buzykaev,[9] V. P. Druzhinin,[9] V. B. Golubev,[9] E. A. Kravchenko,[9] A. P. Onuchin,[9] S. I. Serednyakov,[9] Yu. I. Skovpen,[9] E. P. Solodov,[9] K. Yu. Todyshev,[9] A. N. Yushkov,[9] D. Kirkby,[10] A. J. Lankford,[10] M. Mandelkern,[10] H. Atmacan,[11] J. W. Gary,[11] O. Long,[11] G. M. Vitug,[11] C. Campagnari,[12] T. M. Hong,[12] D. Kovalskyi,[12] J. D. Richman,[12] C. A. West,[12] A. M. Eisner,[13] J. Kroseberg,[13] W. S. Lockman,[13] A. J. Martinez,[13] B. A. Schumm,[13] A. Seiden,[13] D. S. Chao,[14] C. H. Cheng,[14] B. Echenard,[14] K. T. Flood,[14] D. G. Hitlin,[14] P. Ongmongkolkul,[14] F. C. Porter,[14] A. Y. Rakitin,[14] R. Andreassen,[15] Z. Huard,[15] B. T. Meadows,[15] M. D. Sokoloff,[15] L. Sun,[15] P. C. Bloom,[16] W. T. Ford,[16] A. Gaz,[16] U. Nauenberg,[16] J. G. Smith,[16] S. R. Wagner,[16] R. Ayad,[17,*] W. H. Toki,[17] B. Spaan,[18] K. R. Schubert,[19] R. Schwierz,[19] D. Bernard,[20] M. Verderi,[20] P. J. Clark,[21] S. Playfer,[21] D. Bettoni,[22a] C. Bozzi,[22a] R. Calabrese,[22a,22b] G. Cibinetto,[22a,22b] E. Fioravanti,[22a,22b] I. Garzia,[22a,22b] E. Luppi,[22a,22b] L. Piemontese,[22a] V. Santoro,[22a] R. Baldini-Ferroli,[23] A. Calcaterra,[23] R. de Sangro,[23] G. Finocchiaro,[23] P. Patteri,[23] I. M. Peruzzi,[23,†] M. Piccolo,[23] M. Rama,[23] A. Zallo,[23] R. Contri,[24a,24b] E. Guido,[24a,24b] M. Lo Vetere,[24a,24b] M. R. Monge,[24a,24b] S. Passaggio,[24a] C. Patrignani,[24a,24b] E. Robutti,[24a] B. Bhuyan,[25] V. Prasad,[25] M. Morii,[26] A. Adametz,[27] U. Uwer,[27] H. M. Lacker,[28] T. Lueck,[28] P. D. Dauncey,[29] U. Mallik,[30] C. Chen,[31] J. Cochran,[31] W. T. Meyer,[31] S. Prell,[31] A. E. Rubin,[31] A. V. Gritsan,[32] N. Arnaud,[33] M. Davier,[33] D. Derkach,[33] G. Grosdidier,[33] F. Le Diberder,[33] A. M. Lutz,[33] B. Malaescu,[33] P. Roudeau,[33] M. H. Schune,[33] A. Stocchi,[33] G. Wormser,[33] D. J. Lange,[34] D. M. Wright,[34] C. A. Chavez,[35] J. P. Coleman,[35] J. R. Fry,[35] E. Gabathuler,[35] D. E. Hutchcroft,[35] D. J. Payne,[35] C. Touramanis,[35] A. J. Bevan,[36] F. Di Lodovico,[36] R. Sacco,[36] M. Sigamani,[36] G. Cowan,[37] D. N. Brown,[38] C. L. Davis,[38] A. G. Denig,[39] M. Fritsch,[39] W. Gradl,[39] K. Griessinger,[39] A. Hafner,[39] E. Prencipe,[39] R. J. Barlow,[40,‡] G. Jackson,[40] G. D. Lafferty,[40] E. Behn,[41] R. Cenci,[41] B. Hamilton,[41] A. Jawahery,[41] D. A. Roberts,[41] C. Dallapiccola,[42] R. Cowan,[43] D. Dujmic,[43] G. Sciolla,[43] R. Cheaib,[44] D. Lindemann,[44] P. M. Patel,[44,§] S. H. Robertson,[44] P. Biassoni,[45a,45b] N. Neri,[45a] F. Palombo,[45a,45b] S. Stracka,[45a,45b] L. Cremaldi,[46] R. Godang,[46,∥] R. Kroeger,[46] P. Sonnek,[46] D. J. Summers,[46] X. Nguyen,[47] M. Simard,[47] P. Taras,[47] G. De Nardo,[48a,48b] D. Monorchio,[48a,48b] G. Onorato,[48a,48b] C. Sciacca,[48a,48b] M. Martinelli,[49] G. Raven,[49] C. P. Jessop,[50] J. M. LoSecco,[50] W. F. Wang,[50] K. Honscheid,[51] R. Kass,[51] J. Brau,[52] R. Frey,[52] N. B. Sinev,[52] D. Strom,[52] E. Torrence,[52] E. Feltresi,[53a,53b] N. Gagliardi,[53a,53b] M. Margoni,[53a,53b] M. Morandin,[53a] M. Posocco,[53a] M. Rotondo,[53a] G. Simi,[53a] F. Simonetto,[53a,53b] R. Stroili,[53a,53b] S. Akar,[54] E. Ben-Haim,[54] M. Bomben,[54] G. R. Bonneaud,[54] H. Briand,[54] G. Calderini,[54] J. Chauveau,[54] O. Hamon,[54] Ph. Leruste,[54] G. Marchiori,[54] J. Ocariz,[54] S. Sitt,[54] M. Biasini,[55a,55b] E. Manoni,[55a,55b] S. Pacetti,[55a,55b] A. Rossi,[55a,55b] C. Angelini,[56a,56b] G. Batignani,[56a,56b] S. Bettarini,[56a,56b] M. Carpinelli,[56a,56b,¶] G. Casarosa,[56a,56b] A. Cervelli,[56a,56b] F. Forti,[56a,56b] M. A. Giorgi,[56a,56b] A. Lusiani,[56a,56c] B. Oberhof,[56a,56b] A. Perez,[56a] G. Rizzo,[56a,56b] J. J. Walsh,[56a] D. Lopes Pegna,[57] J. Olsen,[57] A. J. S. Smith,[57] F. Anulli,[58a] R. Faccini,[58a,58b] F. Ferrarotto,[58a] F. Ferroni,[58a,58b] M. Gaspero,[58a,58b] L. Li Gioi,[58a] M. A. Mazzoni,[58a] G. Piredda,[58a] C. Bünger,[59] O. Grünberg,[59] T. Hartmann,[59] T. Leddig,[59] H. Schröder,[59,§] C. Voß,[59] R. Waldi,[59] T. Adye,[60] E. O. Olaiya,[60] F. F. Wilson,[60] S. Emery,[61] G. Hamel de Monchenault,[61] G. Vasseur,[61] Ch. Yèche,[61] D. Aston,[62] R. Bartoldus,[62] J. F. Benitez,[62] C. Cartaro,[62] M. R. Convery,[62] J. Dorfan,[62] G. P. Dubois-Felsmann,[62] W. Dunwoodie,[62] M. Ebert,[62] R. C. Field,[62] M. Franco Sevilla,[62] B. G. Fulsom,[62] A. M. Gabareen,[62] M. T. Graham,[62] P. Grenier,[62] C. Hast,[62] W. R. Innes,[62] M. H. Kelsey,[62] P. Kim,[62] M. L. Kocian,[62] D. W. G. S. Leith,[62] P. Lewis,[62] B. Lindquist,[62] S. Luitz,[62] V. Luth,[62] H. L. Lynch,[62] D. B. MacFarlane,[62] D. R. Muller,[62] H. Neal,[62] S. Nelson,[62] M. Perl,[62] T. Pulliam,[62] B. N. Ratcliff,[62] A. Roodman,[62] A. A. Salnikov,[62] R. H. Schindler,[62] A. Snyder,[62] D. Su,[62] M. K. Sullivan,[62] J. Va'vra,[62] A. P. Wagner,[62] W. J. Wisniewski,[62] M. Wittgen,[62] D. H. Wright,[62] H. W. Wulsin,[62] C. C. Young,[62] V. Ziegler,[62] W. Park,[63] M. V. Purohit,[63] R. M. White,[63] J. R. Wilson,[63] A. Randle-Conde,[64] S. J. Sekula,[64] M. Bellis,[65] P. R. Burchat,[65] T. S. Miyashita,[65] E. M. T. Puccio,[65] M. S. Alam,[66] J. A. Ernst,[66] R. Gorodeisky,[67] N. Guttman,[67] D. R. Peimer,[67] A. Soffer,[67] S. M. Spanier,[68] J. L. Ritchie,[69] A. M. Ruland,[69] R. F. Schwitters,[69] B. C. Wray,[69] J. M. Izen,[70] X. C. Lou,[70] F. Bianchi,[71a,71b] D. Gamba,[71a,71b] S. Zambito,[71a,71b] L. Lanceri,[72a,72b] L. Vitale,[72a,72b] F. Martinez-Vidal,[73] A. Oyanguren,[73] P. Villanueva-Perez,[73] H. Ahmed,[74] J. Albert,[74] Sw. Banerjee,[74] F. U. Bernlochner,[74] H. H. F. Choi,[74] G. J. King,[74] R. Kowalewski,[74] M. J. Lewczuk,[74] I. M. Nugent,[74] J. M. Roney,[74] R. J. Sobie,[74] N. Tasneem,[74] T. J. Gershon,[75] P. F. Harrison,[75] T. E. Latham,[75] H. R. Band,[76] S. Dasu,[76] Y. Pan,[76] R. Prepost,[76] and S. L. Wu[76]

(*BABAR* Collaboration)

[1]*Laboratoire d'Annecy-le-Vieux de Physique des Particules (LAPP), Université de Savoie, CNRS/IN2P3, F-74941 Annecy-Le-Vieux, France*
[2]*Universitat de Barcelona, Facultat de Fisica, Departament ECM, E-08028 Barcelona, Spain*
[3a]*INFN Sezione di Bari, I-70126 Bari, Italy*
[3b]*Dipartimento di Fisica, Università di Bari, I-70126 Bari, Italy*
[4]*University of Bergen, Institute of Physics, N-5007 Bergen, Norway*
[5]*Lawrence Berkeley National Laboratory and University of California, Berkeley, California 94720, USA*
[6]*Ruhr Universität Bochum, Institut für Experimentalphysik 1, D-44780 Bochum, Germany*
[7]*University of British Columbia, Vancouver, British Columbia, Canada V6T 1Z1*
[8]*Brunel University, Uxbridge, Middlesex UB8 3PH, United Kingdom*
[9]*Budker Institute of Nuclear Physics, Novosibirsk 630090, Russia*
[10]*University of California at Irvine, Irvine, California 92697, USA*
[11]*University of California at Riverside, Riverside, California 92521, USA*
[12]*University of California at Santa Barbara, Santa Barbara, California 93106, USA*
[13]*University of California at Santa Cruz, Institute for Particle Physics, Santa Cruz, California 95064, USA*
[14]*California Institute of Technology, Pasadena, California 91125, USA*
[15]*University of Cincinnati, Cincinnati, Ohio 45221, USA*
[16]*University of Colorado, Boulder, Colorado 80309, USA*
[17]*Colorado State University, Fort Collins, Colorado 80523, USA*
[18]*Technische Universität Dortmund, Fakultät Physik, D-44221 Dortmund, Germany*
[19]*Technische Universität Dresden, Institut für Kern- und Teilchenphysik, D-01062 Dresden, Germany*
[20]*Laboratoire Leprince-Ringuet, Ecole Polytechnique, CNRS/IN2P3, F-91128 Palaiseau, France*
[21]*University of Edinburgh, Edinburgh EH9 3JZ, United Kingdom*
[22a]*INFN Sezione di Ferrara, I-44100 Ferrara, Italy*
[22b]*Dipartimento di Fisica, Università di Ferrara, I-44100 Ferrara, Italy*
[23]*INFN Laboratori Nazionali di Frascati, I-00044 Frascati, Italy*
[24a]*INFN Sezione di Genova, I-16146 Genova, Italy*
[24b]*Dipartimento di Fisica, Università di Genova, I-16146 Genova, Italy*
[25]*Indian Institute of Technology Guwahati, Guwahati, Assam 781 039, India*
[26]*Harvard University, Cambridge, Massachusetts 02138, USA*
[27]*Universität Heidelberg, Physikalisches Institut, Philosophenweg 12, D-69120 Heidelberg, Germany*
[28]*Humboldt-Universität zu Berlin, Institut für Physik, Newtonstraße 15, D-12489 Berlin, Germany*
[29]*Imperial College London, London, SW7 2AZ, United Kingdom*
[30]*University of Iowa, Iowa City, Iowa 52242, USA*
[31]*Iowa State University, Ames, Iowa 50011-3160, USA*
[32]*Johns Hopkins University, Baltimore, Maryland 21218, USA*
[33]*Laboratoire de l'Accélérateur Linéaire, IN2P3/CNRS et Université Paris-Sud 11, Centre Scientifique d'Orsay, B. P. 34, F-91898 Orsay Cedex, France*
[34]*Lawrence Livermore National Laboratory, Livermore, California 94550, USA*
[35]*University of Liverpool, Liverpool L69 7ZE, United Kingdom*
[36]*Queen Mary, University of London, London, E1 4NS, United Kingdom*
[37]*University of London, Royal Holloway and Bedford New College, Egham, Surrey TW20 0EX, United Kingdom*
[38]*University of Louisville, Louisville, Kentucky 40292, USA*
[39]*Johannes Gutenberg-Universität Mainz, Institut für Kernphysik, D-55099 Mainz, Germany*
[40]*University of Manchester, Manchester M13 9PL, United Kingdom*
[41]*University of Maryland, College Park, Maryland 20742, USA*
[42]*University of Massachusetts, Amherst, Massachusetts 01003, USA*
[43]*Laboratory for Nuclear Science, Massachusetts Institute of Technology, Cambridge, Massachusetts 02139, USA*
[44]*McGill University, Montréal, Québec, Canada H3A 2T8*
[45a]*INFN Sezione di Milano, I-20133 Milano, Italy*
[45b]*Dipartimento di Fisica, Università di Milano, I-20133 Milano, Italy*
[46]*University of Mississippi, University, Mississippi 38677, USA*
[47]*Université de Montréal, Physique des Particules, Montréal, Québec, Canada H3C 3J7*
[48a]*INFN Sezione di Napoli, I-80126 Napoli, Italy*
[48b]*Dipartimento di Scienze Fisiche, Università di Napoli Federico II, I-80126 Napoli, Italy*
[49]*NIKHEF, National Institute for Nuclear Physics and High Energy Physics, NL-1009 DB Amsterdam, The Netherlands*
[50]*University of Notre Dame, Notre Dame, Indiana 46556, USA*

^{51}Ohio State University, Columbus, Ohio 43210, USA

^{52}University of Oregon, Eugene, Oregon 97403, USA

^{53a}INFN Sezione di Padova, I-35131 Padova, Italy

^{53b}Dipartimento di Fisica, Università di Padova, I-35131 Padova, Italy

^{54}Laboratoire de Physique Nucléaire et de Hautes Energies, IN2P3/CNRS, Université Pierre et Marie Curie-Paris6, Université Denis Diderot-Paris7, F-75252 Paris, France

^{55a}INFN Sezione di Perugia, I-06100 Perugia, Italy

^{55b}Dipartimento di Fisica, Università di Perugia, I-06100 Perugia, Italy

^{56a}INFN Sezione di Pisa, I-56127 Pisa, Italy

^{56b}Dipartimento di Fisica, Università di Pisa, I-56127 Pisa, Italy

^{56c}Scuola Normale Superiore di Pisa, I-56127 Pisa, Italy

^{57}Princeton University, Princeton, New Jersey 08544, USA

^{58a}INFN Sezione di Roma, I-00185 Roma, Italy

^{58b}Dipartimento di Fisica, Università di Roma La Sapienza, I-00185 Roma, Italy

^{59}Universität Rostock, D-18051 Rostock, Germany

^{60}Rutherford Appleton Laboratory, Chilton, Didcot, Oxon, OX11 0QX, United Kingdom

^{61}CEA, Irfu, SPP, Centre de Saclay, F-91191 Gif-sur-Yvette, France

^{62}SLAC National Accelerator Laboratory, Stanford, California 94309, USA

^{63}University of South Carolina, Columbia, South Carolina 29208, USA

^{64}Southern Methodist University, Dallas, Texas 75275, USA

^{65}Stanford University, Stanford, California 94305-4060, USA

^{66}State University of New York, Albany, New York 12222, USA

^{67}Tel Aviv University, School of Physics and Astronomy, Tel Aviv 69978, Israel

^{68}University of Tennessee, Knoxville, Tennessee 37996, USA

^{69}University of Texas at Austin, Austin, Texas 78712, USA

^{70}University of Texas at Dallas, Richardson, Texas 75083, USA

^{71a}INFN Sezione di Torino, I-10125 Torino, Italy

^{71b}Dipartimento di Fisica Sperimentale, Università di Torino, I-10125 Torino, Italy

^{72a}INFN Sezione di Trieste, I-34127 Trieste, Italy

^{72b}Dipartimento di Fisica, Università di Trieste, I-34127 Trieste, Italy

^{73}IFIC, Universitat de Valencia-CSIC, E-46071 Valencia, Spain

^{74}University of Victoria, Victoria, British Columbia, Canada V8W 3P6

^{75}Department of Physics, University of Warwick, Coventry CV4 7AL, United Kingdom

^{76}University of Wisconsin, Madison, Wisconsin 53706, USA

We study the decay $\bar{B}^0 \to \Lambda_c^+ \bar{p} \pi^+ \pi^-$, reconstructing the Λ_c^+ baryon in the $pK^-\pi^+$ mode, using a data sample of 467×10^6 $B\bar{B}$ pairs collected with the *BABAR* detector at the PEP-II storage rings at SLAC. We measure branching fractions for decays with intermediate Σ_c baryons to be $\mathcal{B}[\bar{B}^0 \to \Sigma_c(2455)^{++} \bar{p} \pi^-] = (21.3 \pm 1.0 \pm 1.0 \pm 5.5) \times 10^{-5}$, $\mathcal{B}[\bar{B}^0 \to \Sigma_c(2520)^{++} \bar{p} \pi^-] = (11.5 \pm 1.0 \pm 0.5 \pm 3.0) \times 10^{-5}$, $\mathcal{B}[\bar{B}^0 \to \Sigma_c(2455)^0 \bar{p} \pi^+] = (9.1 \pm 0.7 \pm 0.4 \pm 2.4) \times 10^{-5}$, and $\mathcal{B}[\bar{B}^0 \to \Sigma_c(2520)^0 \bar{p} \pi^+] = (2.2 \pm 0.7 \pm 0.1 \pm 0.6) \times 10^{-5}$, where the uncertainties are statistical, systematic, and due to the uncertainty on the $\Lambda_c^+ \to pK^-\pi^+$ branching fraction, respectively. For decays without $\Sigma_c(2455)$ or $\Sigma_c(2520)$ resonances, we measure $\mathcal{B}[\bar{B}^0 \to \Lambda_c^+ \bar{p} \pi^+ \pi^-]_{\text{non-}\Sigma_c} = (79 \pm 4 \pm 4 \pm 20) \times 10^{-5}$. The total branching fraction is determined to be $\mathcal{B}[\bar{B}^0 \to \Lambda_c^+ \bar{p} \pi^+ \pi^-]_{\text{total}} = (123 \pm 5 \pm 7 \pm 32) \times 10^{-5}$. We examine multibody mass combinations in the resonant three-particle $\Sigma_c \bar{p} \pi$ final states and in the four-particle $\Lambda_c^+ \bar{p} \pi^+ \pi^-$ final state, and observe different characteristics for the $\bar{p}\pi$ combination in neutral versus doubly charged Σ_c decays.

*Now at the University of Tabuk, Tabuk 71491, Saudi Arabia.

†Also with Università di Perugia, Dipartimento di Fisica, Perugia, Italy.

‡Now at the University of Huddersfield, Huddersfield HD1 3DH, UK.

§Deceased.

‖Now at University of South Alabama, Mobile, AL 36688, USA.

¶Also with Università di Sassari, Sassari, Italy.

I. INTRODUCTION

Decays of *B* mesons into final states with baryons account for $(6.8 \pm 0.6)\%$ [1] of all *B*-meson decays. Notwithstanding their significant production rate, the baryon production mechanism in *B*-meson decays is poorly understood. Theoretical models of *B*-meson baryonic decays are currently limited to rough estimates of the branching fractions and basic interpretations of the decay mechanisms [2–6]. Additional experimental information may help to clarify the underlying dynamics.

In this paper, we present a measurement of the *B*-meson baryonic decay[1] $\bar{B}^0 \rightarrow \Lambda_c^+ \bar{p} \pi^+ \pi^-$. The Λ_c^+ baryon is observed through its decays to the $pK^-\pi^+$ final state. The study is performed using a sample of e^+e^- annihilation data collected at the mass of the $\Upsilon(4S)$ resonance with the *BABAR* detector at the SLAC National Accelerator Laboratory. We include a study of the production of this final state through intermediate Σ_c^{++} and Σ_c^0 resonances. The *sPlot* technique [7] is used to examine multibody mass combinations within the $\Sigma_c \bar{p} \pi$ final states. We account for background from sources such as $B \rightarrow D p \bar{p}(n\pi)$ and $B^- \rightarrow \Sigma_c^+ \bar{p} \pi^-$, which were not considered in previous studies [8,9]. In addition, we extract the four-body nonresonant branching fraction and examine two- and three-body mass combinations within the four-body $\Lambda_c^+ \bar{p} \pi^+ \pi^-$ final state. The $\bar{B}^0 \rightarrow \Lambda_c^+ \bar{p} \pi^+ \pi^-$ decay has previously been studied by the CLEO [8] and Belle [9] Collaborations using data samples of 9.17 fb^{-1} and 357 fb^{-1}, respectively. The present work represents the first study of this decay mode from *BABAR*.

Section II provides a brief description of the *BABAR* detector and data sample. The basic event selection procedure is described in Sec. III. Section IV presents the method used to extract results for channels that proceed via intermediate Σ_c baryons. The corresponding results for channels that do not proceed via Σ_c baryons are presented in Sec. V. Section VI presents the method used to determine signal reconstruction efficiencies, Sec. VII the branching fraction results, Sec. VIII the evaluation of systematic uncertainties, and Sec. IX the final results. A summary is given in Sec. X.

II. *BABAR* DETECTOR AND DATA SAMPLE

The data sample used in this analysis was collected with the *BABAR* detector at the PEP-II asymmetric-energy e^+e^- storage ring at SLAC. PEP-II operates with a 9 GeV e^- and a 3.1 GeV e^+ beam resulting in a center-of-mass energy equal to the $\Upsilon(4S)$ mass of 10.58 GeV/c^2. The collected data sample contains 467×10^6 $B\bar{B}$ pairs, which corresponds to an integrated luminosity of 426 fb^{-1}.

---

[1]The use of charge conjugate decays is implied throughout this paper.

The *BABAR* detector [10] measures charged-particle tracks with a five-layer double-sided silicon vertex tracker (SVT) surrounded by a 40-layer drift chamber (DCH). Charged particles are identified using specific ionization energy measurements in the SVT and DCH, as well as Cherenkov radiation measurements in an internally reflecting ring imaging Cherenkov detector (DIRC). These detectors are located within the 1.5 T magnetic field of a superconducting solenoid.

Using information from the SVT, the DCH, and the DIRC for a particular track, the probability for a given particle hypothesis is calculated from likelihood ratios. The identification efficiency for a proton is larger than 90%, with the probability of misidentifying a kaon or pion as a proton between 3% and 15% depending on the momentum. For a kaon, the identification efficiency is 90%, with the probability of misidentifying a pion or proton as a kaon between 5% and 10%. The identification efficiency for a pion is larger than 95%, with the probability of misidentifying a kaon or proton as a pion between 5% and 30%.

Monte Carlo (MC) simulated events are produced with an $e^+e^- \rightarrow B\bar{B}$ event simulation based on the EvtGen program [11] and an $e^+e^- \rightarrow u\bar{u}$, $d\bar{d}$, $s\bar{s}$, $c\bar{c}$ event simulation based on the JETSET program [12]. Generated events are processed in a GEANT4 [13] simulation of the *BABAR* detector. MC-generated events are studied for generic background contributions as well as for specific signal and background modes. Baryonic *B*-meson decays are generated assuming that their daughters are distributed uniformly in phase space.

III. EVENT SELECTION

The signal mode is reconstructed in the decay chain $\bar{B}^0 \rightarrow \Lambda_c^+ \bar{p} \pi^+ \pi^-$ with $\Lambda_c^+ \rightarrow pK^-\pi^+$. All final-state particles are required to have well-defined tracks in the SVT and DCH. Kaons and protons, as well as pions from the Λ_c^+ decay, are required to pass likelihood selectors based on information from the SVT, DCH, and DIRC. For pion candidates from the $\bar{B}^0$ decay, a well-reconstructed track is required.

To form a Λ_c^+ candidate, the p, K^-, and π^+ candidates are fitted to a common vertex and a χ^2 probability greater than 0.1% is required for the vertex fit. To form a $\bar{B}^0$ candidate, the Λ_c^+ candidate is constrained to its nominal mass value and combined with an antiproton and two pions with opposite charge. The mass constraint value differs between events from data and MC. For the MC events a nominal Λ_c^+ mass of $m_{\Lambda_c^+}^{\text{MC}} = 2284.9$ MeV/c^2 is chosen; this corresponds to the mass value used in the MC generation and to the value from fits to reconstructed MC events. For data, χ^2 fits are performed on the $m(pK^-\pi^+)$ invariant mass distribution to find the nominal Λ_c^+ mass. The fits are performed for each of the six distinct *BABAR* run periods. The results are found to vary between $m_{\Lambda_c^+}^{\text{data}} = (2285.55 \pm 0.18)$ MeV/c^2 and $m_{\Lambda_c^+}^{\text{data}} = (2285.62 \pm 0.22)$ MeV/c^2,

where the uncertainties are statistical. All invariant mass values are found to be consistent. The average result $m_{\Lambda_c^+}^{\text{data}} = 2285.6$ MeV/c^2 is used as the nominal value for the mass constraint in data.

Only candidates within a 25 MeV/c^2 mass window centered on the nominal Λ_c^+ mass $m_{\Lambda_c^+}^{\text{data}}$ (or $m_{\Lambda_c^+}^{\text{MC}}$ for simulated events) are retained. The entire decay chain is refitted, requiring that the direct $\bar{B}^0$ daughters originate from a common vertex and that the χ^2 probability for the $\bar{B}^0$ vertex fit exceeds 0.1%.

The decays $B \to D p \bar{p} (n\pi)$ with $n = 1, 2$, which are described in more detail in Sec. IVA, can contribute a signal-like background through rearrangement of the final-state particles and are denoted ''peaking background'' in the following. To suppress these events, symmetric vetoes of ± 20 MeV/c^2 around the nominal D^0 and D^+ mass values [1] are applied in the distributions of the invariant masses $m([K^-\pi^+]_{\Lambda_c^+}[\pi^-\pi^+]_{\bar{B}^0})$, $m([K^-\pi^+]_{\Lambda_c^+}[\pi^+]_{\bar{B}^0})$, and $m([K^-\pi^+]_{\Lambda_c^+})$, where subscripts denote the mother candidate of the particles.

To separate $\bar{B}^0$ signal events from combinatorial background, two variables are used. The $\bar{B}^0$ invariant mass is defined as $m_{\text{inv}} = \sqrt{E_{\bar{B}^0}^2 - \mathbf{p}_{\bar{B}^0}^2}$, with the four-momentum vector of the $\bar{B}^0$ candidate $(E_{\bar{B}^0}, \mathbf{p}_{\bar{B}^0})$ measured in the laboratory frame. The energy-substituted mass is defined in the laboratory frame as $m_{\text{ES}} = \sqrt{(s/2 + \mathbf{p}_i \cdot \mathbf{p}_{\bar{B}^0})^2/E_i^2 - \mathbf{p}_{\bar{B}^0}^2}$, with $\sqrt{s}$ the center-of-mass energy and $(E_i, \mathbf{p}_i)$ the four-momentum vector of the initial e^+e^- system measured in the laboratory frame. For both variables, genuine $\bar{B}^0$ decays are centered at the $\bar{B}^0$-meson mass. In MC, these variables exhibit a negligible correlation for genuine $\bar{B}^0$ mesons.

To suppress combinatorial background, $\bar{B}^0$ candidates are required to satisfy $m_{\text{ES}} \in [5.272, 5.285]$ GeV/c^2.
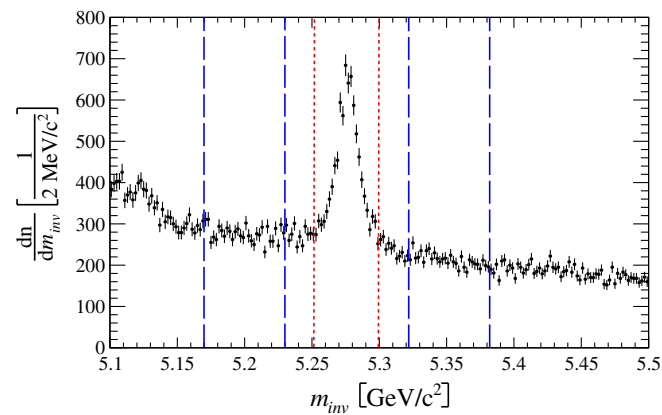

FIG. 1 (color online). Distribution of the invariant mass $m_{\text{inv}}(\Lambda_c^+ \bar{p} \pi^+ \pi^-)$ for events with m_{ES} in the region [5.272, 5.285] GeV/c^2. The red dotted lines indicate the signal region and the blue dashed lines the sideband regions. Higher multiplicity modes, such as $B \to \Lambda_c^+ \bar{p} \pi^+ \pi^- \pi$, appear for $m_{\text{inv}} < 5.14$ GeV/c^2.

Figure 1 shows the m_{inv} distribution after applying all of the above selection criteria. The dashed lines show sideband regions $m_{\text{inv}} \in [5.170, 5.230]$ and $m_{\text{inv}} \in [5.322, 5.382]$, used to study background characteristics; both sideband regions are combined into a single sideband region.

The analysis is separated into two parts: (i) the measurement of the four signal decays via intermediate $\Sigma_c(2455, 2520)$ resonances, i.e., $\bar{B}^0 \to \Sigma_c(2455)^{++} \bar{p} \pi^-$, $\bar{B}^0 \to \Sigma_c(2520)^{++} \bar{p} \pi^-$, $\bar{B}^0 \to \Sigma_c(2455)^0 \bar{p} \pi^+$, and $\bar{B}^0 \to \Sigma_c(2520)^0 \bar{p} \pi^+$, and (ii) the measurement of all other decays into the four-body final state $\Lambda_c^+ \bar{p} \pi^+ \pi^-$, which are denoted as *non-Σ_c signal events* in the following.

IV. $\bar{B}^0 \to \Sigma_c^{++,0} \bar{p}\pi^{\mp}$ ANALYSIS

Decays via resonant intermediate states with Σ_c resonances are studied in the two-dimensional planes spanned by m_{inv} and the invariant Σ_c candidate invariant mass $m(\Lambda_c^+ \pi^+)$ for decays with $\Sigma_c(2455, 2520)^{++}$ and $m(\Lambda_c^+ \pi^-)$ for decays with $\Sigma_c(2455, 2520)^0$. In the following the like-sign $\Lambda_c \pi$ invariant mass is denoted as m_{++} and the opposite-sign invariant mass as m_{+-}. If both invariant masses are referred to, we use the notation $m_{+\pm}$. For intermediate $\Sigma_c(2455, 2520)^{++,0}$ states, $\mathcal{B}[\Sigma_c \to \Lambda_c^+ \pi] \approx 100\%$ is assumed [1].

We perform fits in both planes $m_{\text{inv}}:m_{++}$ and $m_{\text{inv}}:m_{+-}$ to extract the signal yields for the decays via the Σ_c resonances. Background contributions are vetoed when feasible. We distinguish between different signal and remaining background contributions by using separate probability density functions (PDFs) for each signal and background component. We use analytical PDFs as well as discrete histogram PDFs. The PDFs are validated using data from the sideband regions and from MC samples. The different, combined PDFs are fitted to the $m_{\text{inv}}:m_{++}$ and $m_{\text{inv}}:m_{+-}$ planes and the resulting covariance matrices of the fits are used to calculate *sPlot* [7] distributions of signal events.

Figures 2(a) and 2(b) show the m_{++} and m_{+-} distributions, respectively, after applying the selection criteria as described in Sec. III. Signal contributions from the $\Sigma_c(2455)^{++}$, $\Sigma_c(2520)^{++}$, and $\Sigma_c(2455)^0$ resonances are observed and a contribution from events with a $\Sigma_c(2800)^{++}$ resonance is visible. The doubly charged Σ_c^{++} resonances are seen to contribute larger numbers of events than the neutral Σ_c^0 resonances. The resonant structures sit on top of combinatorial background and peaking background events as well as non-Σ_c signal events. The latter are distributed in $m(\Lambda_c^+ \pi^{\pm})$ like combinatorial background events.

A. Background sources

The main source for combinatorial background events is other B decays, while 20% originate from $e^+e^- \to c\bar{c}$ events. Combinatorial events do not exhibit peaking structures in the distributions of the signal variables under study.
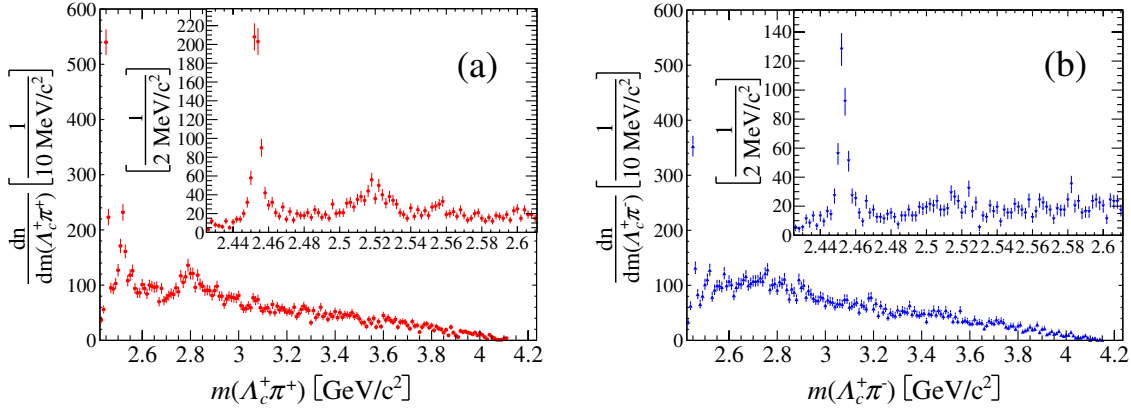
FIG. 2 (color online). Event distributions in $m(\Lambda_c^+ \pi^+)$ (a) and $m(\Lambda_c^+ \pi^-)$ (b) for events in the signal region of Fig. 1. The inserts show the low invariant mass regions.

In contrast, other sources of background do exhibit peaking structures, and are treated separately.

1. $B \to D p \bar{p} (n\pi)$

Decays of the type $B \to D p \bar{p} (n\pi)$ with $D \to K^- (m\pi)$, where $n + m = 3$, can have the same final-state particles as signal decays. Rearrangement of the final-state particles can yield a fake Λ_c^+ candidate, while the $\bar{B}^0$ candidate is essentially a genuine $\bar{B}^0$ suppressed only by the Λ_c^+ selection. Because these events represent fully reconstructed genuine B-meson decays, they are distributed like signal events in the m_{inv} and m_{ES} variables. Table I shows the relevant decay modes and their misreconstruction rate as signal. Furthermore, these events can also be misreconstructed as higher Σ_c resonances in the $\Lambda_c^+ \pi$ invariant masses. Figure 3 shows the distributions of the MC-simulated background modes in the $m_{inv}:m_{++}$ and $m_{inv}:m_{+-}$ planes. Additionally, $\bar{B}^0 \to D^+ p\bar{p}\pi^-$ events with $D^+ \to K^- \pi^+ \pi^+$ have a minimum invariant mass in m_{++} of $m(D^+ p) \approx 2.808$ GeV/c^2 and can introduce background in the study of events with intermediate $\Sigma_c(2800)^{++}$ resonances.

From the misreconstruction efficiency determined from signal MC events and scaled with the measured branching fractions [14], 167 ± 20 background events are expected to contribute as signal. To suppress these events, veto regions are set to 20 MeV/c^2 around the nominal D^0 and D^+ masses [1] in $m(K^- \pi^+)$, $m(K^- \pi^+ \pi^+)$, and $m(K^- \pi^+ \pi^+ \pi^-)$, with the resulting suppression rates given in Table I. A systematic uncertainty is assigned to account for the remaining background events. No distortions are found in other variables due to the vetoes. Note that $\bar{B}^0 \to D^0 p\bar{p}\pi^+ \pi^-$ events with $D^0 \to K^- \pi^+$ rearranged to $\bar{B}^0 \to [\pi^- \pi^+ \bar{p}[p]_{\bar{B}^0}[K^- \pi^+]_{D^0}]_{fake \Lambda_c^+}$ do not contribute peaking background because the selection requirement on $m(pK^- \pi^+)_{\Lambda_c^+}$ effectively vetoes these events.

2. $\bar{B}^0 \to (c\bar{c})\bar{K}^{*0} \pi^+ \pi^-$

Decays via charmonia, such as $\bar{B}^0 \to (c\bar{c})\bar{K}^{*0} \pi^+ \pi^-$ with $(c\bar{c}) \to p\bar{p}$ and $\bar{K}^{*0} \to K^- \pi^+$, or $\bar{B}^0 \to (c\bar{c})\bar{K}^{*0}$ with $(c\bar{c}) \to p\bar{p}\pi^+ \pi^-$, can also produce the same final-state particles as signal events. We observe no indication of such contributions in data in the relevant combinations of $\bar{B}^0$ daughters or in signal MC events when scaling the
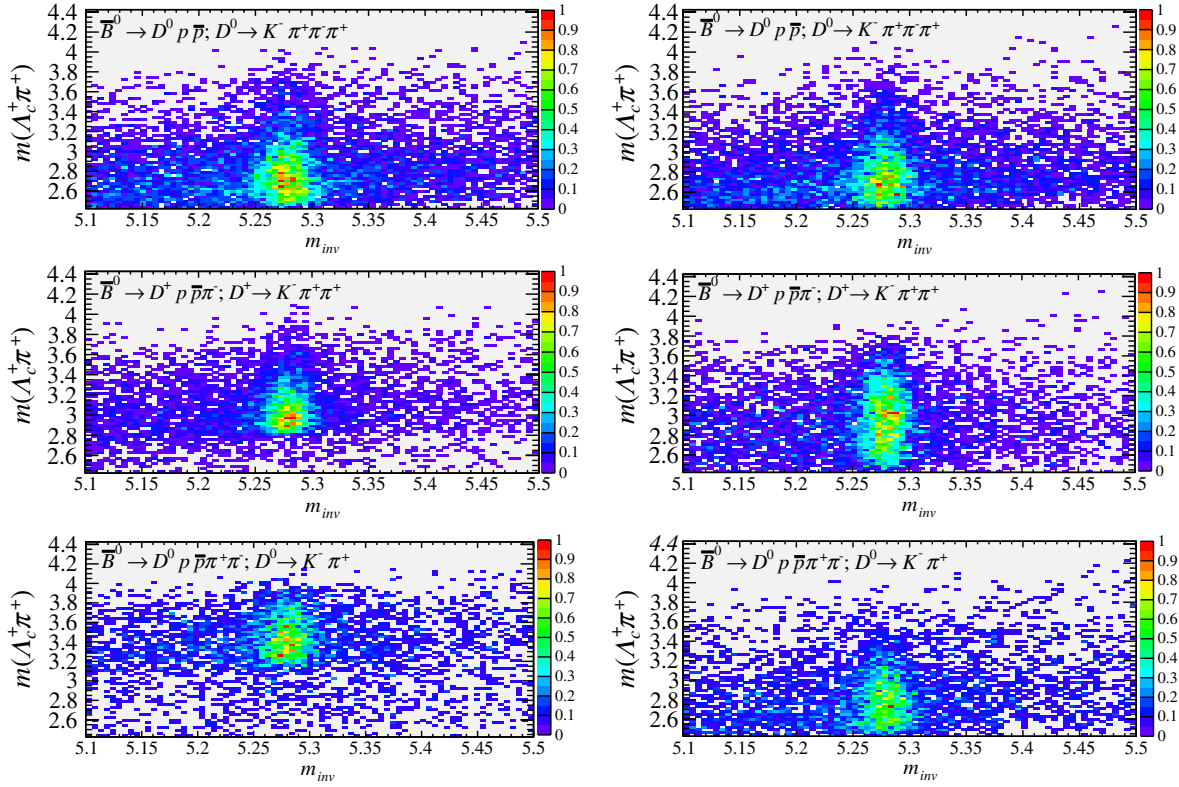
TABLE I. Efficiencies for reconstructing $\bar{B}^0 \to D p \bar{p}(n\pi)$ events as signal decays by rearranging the final-state particles in signal-like combinations. In the fake signal reconstruction, the subscript particles denote the actual mother. The quantity $n_{expected}$ gives the number of fake signal events without the D-meson veto (see text), ε_{Cut} gives the efficiencies of the vetoes, and $n_{remaining}$ gives the expected number of remaining fake events in the signal regions after applying the vetoes. The $\bar{B}^0 \to D p \bar{p}(n\pi)$ branching fractions are taken from Ref. [14] and the D^0/D^+ branching fractions from Ref. [1].

Decay mode	Fake signal	$\varepsilon_{\bar{B}^0 \to \Lambda_c^+ \bar{p}\pi^+ \pi^-}$	$n_{expected}$	ε_{Cut}	$n_{remaining}$
$\bar{B}^0 \to D^0 p\bar{p}$ $D^0 \to K^- \pi^+ \pi^- \pi^+$	$\bar{B}^0_{fake} \to [\bar{p}[p]_{\bar{B}^0}[K^- \pi^+]_{fake\Lambda_c^+} \pi^- \pi^+]_{D^0}$	$(6.79 \pm 0.19) \times 10^{-3}$	26.0	99.3%	0.3
$\bar{B}^0 \to D^+ p\bar{p}\pi^-$ $D^+ \to K^- \pi^+ \pi^+$	$\bar{B}^0_{fake} \to [\pi^- \bar{p}[p]_{\bar{B}^0}[K^- \pi^+]_{fake\Lambda_c^+} \pi^+]_{D^+}$	$(7.28 \pm 0.17) \times 10^{-3}$	103.0	98.8%	1.0
$\bar{B}^0 \to D^0 p\bar{p}\pi^+ \pi^-$ $D^0 \to K^- \pi^+$	$\bar{B}^0_{fake} \to [\pi^- \bar{p}[p\pi^+]_{\bar{B}^0}[K^-]_{fake\Lambda_c^+} \pi^+]_{D^0}$	$(4.19 \pm 0.15) \times 10^{-3}$	22.5	96.9%	0.2
$\bar{B}^0 \to D^{*+} p\bar{p}\pi^+$ $D^{*+} \to D^0 \pi^+$ $D^0 \to K^- \pi^+$	$\bar{B}^0_{fake} \to \pi^+ \bar{p}[p[[K^- \pi^+]_{D^0}]_{fake\Lambda_c^+} \pi^+]_{D^{*+}}$	$(2.44 \pm 0.12) \times 10^{-3}$	13.4	96.9%	0.1

FIG. 3 (color online).   Simulated events with $\bar{B}^0 \to Dp\bar{p}(n\pi)$ decays misidentified as signal decays in the m_{inv}:m_{++} plane (left column) and m_{inv}:m_{+-} plane (right column). The MC-generated events are reconstructed as $\bar{B}^0 \to \Lambda_c^+ \bar{p}\pi^+\pi^-$. The color scale indicates the relative contents of a bin compared to the maximally occupied bin.

misreconstruction efficiencies with the measured branching fractions [1]. We neglect these events, but assign a corresponding systematic uncertainty (see Sec. VIII).

3. $B^- \to \Sigma_c^+ \bar{p}\pi^-$

Events from $B^- \to \Sigma_c^+ \bar{p}\pi^-$ decays with $\Sigma_c(2455)^+ \to \Lambda_c^+ \pi^0$ or $\Sigma_c(2520)^+ \to \Lambda_c^+ \pi^0$ are found to have a signal-like shape in m_{inv} and m_{++}. Because of the low-momentum π^0 daughters in the $\Sigma_c(2455, 2520)^+$ center-of-mass systems, fake $\Sigma_c(2455, 2520)^{++}$ can be generated by replacing the π^0 with a π^+ from the B^+. Figure 4 shows the

distributions of MC-generated events. These events cluster in the m_{inv} signal region as well as in m_{++} in the $\Sigma_c(2455)^{++}$ and $\Sigma_c(2520)^{++}$ signal regions. A correlation between m_{inv} and m_{++} is apparent. No significant structures are found in MC-generated events with nonresonant $B^- \to \Lambda_c^+ \bar{p}\pi^-\pi^0$ or with $B^- \to \Sigma_c(2800)^+ \bar{p}\pi^-$ events due to the softer momentum constraints on the π^0.

4. Combinatorial background with genuine Σ_c events

In both MC and data-sideband events, combinatorial background events with genuine $\Sigma_c(2455, 2520)^{++,0}$
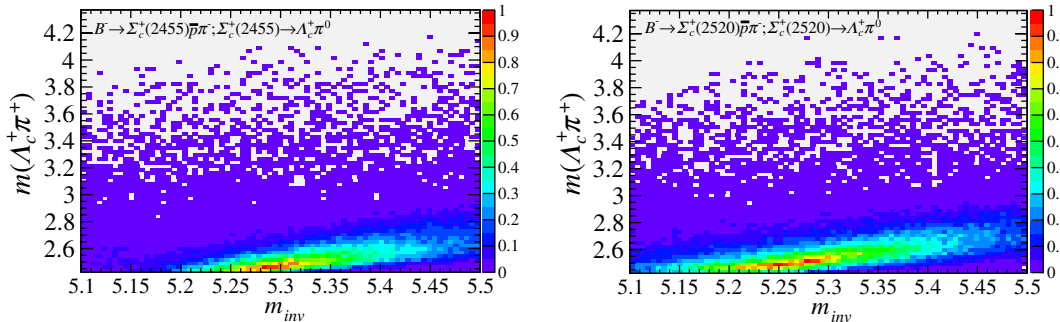

FIG. 4 (color online).   Simulated events with $B^- \to \Sigma_c(2455)^+ \bar{p}\pi^-$ (left) and $B^- \to \Sigma_c(2520)^+ \bar{p}\pi^-$ (right) decays, where $\Sigma_c^+ \to \Lambda_c^+ \pi^0$ decays are reconstructed as $\Sigma_c^{++} \to \Lambda_c^+ \pi^+$; these events accumulate in the signal regions of m_{inv} and in m_{++}. The MC-generated events are reconstructed as $\bar{B}^0 \to \Lambda_c^+ \bar{p}\pi^+\pi^-$. The color scale indicates the relative contents of a bin compared to the maximally occupied bin.

resonances are found to be distributed differently than purely combinatorial background events without Σ_c resonances. These events produce a signal-like structure in m_{++} or m_{+-}, but are distributed in m_{inv} similarly to purely combinatorial background. However, since combinatorial background events with genuine $\Sigma_c(2455, 2520)^{++,0}$ resonances scale differently in m_{inv} than purely combinatorial background events, no simple combined PDF can be constructed. Thus, both combinatorial background sources are treated as separate background classes.

5. $\bar{B}^0 \to \Lambda_c^+ \bar{p} \pi^+ \pi^-$ events without a Σ_c signal

Events also appear as background in the $m_{+\pm}$ distribution when they contain decays into the four-body final state $\bar{B}^0 \to \Lambda_c^+ \bar{p} \pi^+ \pi^-$, not via the signal Σ_c resonance. For example, decays such as $\bar{B}^0 \to \Sigma_c^{++} \bar{p} \pi^-$ are distributed as background to $\bar{B}^0 \to \Sigma_c^0 \bar{p} \pi^+$ events in m_{+-} but as signal in m_{inv}. Therefore, decays to $\bar{B}^0 \to \Lambda_c^+ \bar{p} \pi^+ \pi^-$ not cascading via the signal resonance are included as a background class.

B. Fit strategy

The signal yields of resonant decays are determined in binned maximum-likelihood fits to the two-dimensional distributions m_{inv}:m_{++} and m_{inv}:m_{+-}. Since background events from $B^- \to \Sigma_c^+ \bar{p} \pi^-$ decays are distributed similarly to signal events in all examined variables, one-dimensional measurements of the signal yield will not suffice. By extracting the signal yield in the m_{inv}:$m_{+\pm}$ plane,

we exploit the fact that the distributions of $B^- \to \Sigma_c(2455, 2520)^+ \bar{p} \pi^-$ events are more correlated in these variables than signal events.

1. Type of PDFs

Signal and background sources are divided into two classes of probability density functions. Background sources without significant correlations between m_{inv} and $m_{+\pm}$ are described with analytical PDFs; independent analytical PDFs are used for each of the two variables and a combined two-dimensional PDF is formed by multiplication of the one-dimensional functions. Signal and background sources with correlations between m_{inv} and $m_{+\pm}$ are described with binned histogram PDFs $H_i = S_i \cdot h_i(m_{\mathrm{inv}}, m_{+\pm})$. For each source, a histogram $h_i(m_{\mathrm{inv}}, m_{+\pm})$ is generated from MC events, which takes correlations into account by design. Each histogram h_i is scaled with a parameter S_i, which is allowed to float in the fit. Histogram PDFs are used for all resonant signal decays and peaking background decays $B^- \to \Sigma_c(2455, 2520)^+ \bar{p} \pi^-$.

In the fits to the two-dimensional distributions, the integrals of the analytical PDFs for each bin are calculated. Table II lists the PDFs and indicates whether they are included in the fit to m_{inv}:m_{++} for $\bar{B}^0 \to \Sigma_c^{++} \bar{p} \pi^-$ events or in the fit to m_{inv}:m_{+-} for $\bar{B}^0 \to \Sigma_c^0 \bar{p} \pi^+$ events.

2. Histogram PDF verification

When using a histogram PDF in fits, results prove to be sensitive to differences between data events and

TABLE II. The PDF types for signal and background sources as defined in Sec. IV B (see text for details). In the second column, S_i denote scaling factors, h_i histograms, and X_i, Y_i, BW_i analytical functions as described in the text. The third and fourth columns indicate in which global fit to the planes m_{inv}:m_{++} or m_{inv}:m_{+-} a particular PDF is included.

Mode	PDF	m_{inv}:m_{++}	m_{inv}:m_{+-}
$\bar{B}^0 \to \Sigma_c(2455)^{++} \bar{p} \pi^-$	$H_{\Sigma_c(2455)^{++}} = S_{\Sigma_c(2455)^{++}} \cdot h_{\Sigma_c(2455)^{++}}$	$\surd$	
$\bar{B}^0 \to \Sigma_c(2520)^{++} \bar{p} \pi^-$	$H_{\Sigma_c(2520)^{++}} = S_{\Sigma_c(2520)^{++}} \cdot h_{\Sigma_c(2520)^{++}}$	$\surd$	
$\bar{B}^0 \to \Sigma_c(2455)^0 \bar{p} \pi^+$	$H_{\Sigma_c(2455)^0} = S_{\Sigma_c(2455)^0} \cdot h_{\Sigma_c(2455)^0}$		$\surd$
$\bar{B}^0 \to \Sigma_c(2520)^0 \bar{p} \pi^+$	$H_{\Sigma_c(2520)^0} = S_{\Sigma_c(2520)^0} \cdot h_{\Sigma_c(2520)^0}$		$\surd$
$B^- \to \Sigma_c(2455)^+ \bar{p} \pi^-$	$BG_{\Sigma_c(2455)^+} = S_{\Sigma_c(2455)^+} \cdot h_{\Sigma_c(2455)^+}$	$\surd$	
$B^- \to \Sigma_c(2520)^+ \bar{p} \pi^-$	$BG_{\Sigma_c(2520)^+} = S_{\Sigma_c(2520)^+} \cdot h_{\Sigma_c(2520)^+})$	$\surd$	
Combinatorial background	$BG_{\mathrm{Combi\,Bkg}} = S_{\mathrm{Combi\,Bkg}}$ $\times Y_{\mathrm{Combi\,Bkg}}(m_{+\pm}; p, q; e_{\mathrm{up}}, e_{\mathrm{low}})$ $\times X^{\mathrm{Chebyshev}}_{\mathrm{Combi\,Bkg}}(m_{\mathrm{inv}}; b)$	$\surd$	$\surd$
Combinatorial background with genuine Σ_c	$BG_{\mathrm{Combi\,Bkg\,w\,}\Sigma_c} = S_{\mathrm{Combi\,Bkg\,w\,}\Sigma_c}$ $\times BW_{\mathrm{Combi\,Bkg\,w\,}\Sigma_c}(m_{+\pm}; \mu, \Gamma)$ $\times X^{\mathrm{Chebyshev}}_{\mathrm{Combi\,Bkg\,w\,}\Sigma_c}(m_{\mathrm{inv}}; b)$	$\surd$	$\surd$
non-Σ_c $B^0 \to \Lambda_c^+ \bar{p} \pi^+ \pi^-$	$BG_{\mathrm{non-}\Sigma_c} = S_{\mathrm{non-}\Sigma_c} \times Y_{\mathrm{non-}\Sigma_c}(m_{+\pm}; p, q, r; e_{\mathrm{psb}})$ $\times X^{\mathrm{Gauss}}_{\mathrm{non-}\Sigma_c}(m_{\mathrm{inv}}; \mu, \sigma[m_{+\pm}; a_\sigma, b_\sigma, c_\sigma])$	$\surd$	$\surd$

MC-generated events. As a cross-check, the projections onto m_{inv} are compared between data and MC simulation. The distributions are fitted using a Gaussian function to describe signal events. The means differ between data and MC by $\Delta = (2.30 \pm 0.25)$ MeV/c^2. The mass shift does not depend on the Λ_c^+ candidate selection or on $m_{+\pm}$. The most probable explanation for the difference is an underestimation of the SVT material in the simulation, as studied in detail in Ref. [15]. Baryonic decays are especially affected by this issue, since heavier particles such as protons suffer more from such an underestimation compared to lighter particles. In each MC event, the baryon momenta $|\vec{p}_{P_{\Lambda_c^+}}|$ and $|\vec{p}_{P_{\bar{B}^0}}|$ are therefore increased by 2.30 MeV/c and the particle energy is adjusted accordingly.

In the $m_{+\pm}$ distributions, the means of the masses of the $\Sigma_c(2455)^{++,0}$ baryons differ between data and MC by $\Delta m = (0.441 \pm 0.095)$ MeV/c^2. This effect originates from outdated $\Sigma_c(2455)$ mass inputs in the MC generation, and so this shift is not covered by the correction for detector density. $\Sigma_c(2455)$ events are especially sensitive to such mass differences due to their narrow width. The effect is taken into account by shifting each MC event in $m_{+\pm}$ by $+0.441$ GeV/c^2. The fully corrected data sets are used to generate the histogram PDFs employed in the fits to data.

3. Combinatorial background PDF

The combinatorial background is described by the PDF $\text{BG}_{\text{Combi Bkg}}$ term given in Table II. It consists of two separable functions: for m_{inv} we use a first-order Chebyshev polynomial $\text{X}_{\text{Combi Bkg w }\Sigma_c}^{\text{Chebyshev}}(m_{\text{inv}}; b)$ with a slope parameter b, and for $m_{+\pm}$ a phenomenological function,

$$\begin{aligned}
\text{Y}_{\text{Combi Bkg}}&(m_{+\pm}; p, q; e_{\text{up}}, e_{\text{low}}) \\
&= (c - m_{+\pm})^p \cdot (m_{+\pm} - e_{\text{low}})^q \cdot e_{\text{up}}.
\end{aligned} \quad (1)$$

The upper and lower phase-space boundaries in $m_{+\pm}$ are constants $e_{\text{low}} = 2.4249$ GeV/c^2 and $e_{\text{up}} = 4.215$ GeV/c^2. The phenomenological constant $c = 4.108$ GeV/c^2 is obtained from MC and, for estimating a systematic uncertainty, varied within the values found in MC. The exponent terms p and q are allowed to float in the fits to MC and data. In Table II, $S_{\text{Combi Bkg}}$ is the overall scaling parameter of the combinatorial background PDF.

4. Combinatorial background with genuine Σ_c PDF

Combinatorial background events with genuine Σ_c resonances are described by uncorrelated functions in m_{inv} and $m_{+\pm}$. A first-order Chebyshev polynomial $\text{X}_{\text{Combi Bkg w }\Sigma_c}^{\text{Chebyshev}}$ in m_{inv} is multiplied by a nonrelativistic Breit-Wigner function in $m_{+\pm}$,

$$\text{BW}_{\text{Combi Bkg w }\Sigma_c}(m_{+\pm}; \mu, \Gamma) = \frac{1}{\pi \cdot [(m_{+\pm} - \mu)^2 + (\frac{\Gamma}{2})^2]}, \quad (2)$$

with mean μ, width Γ, and an overall scaling factor $S_{\text{Combi Bkg w }\Sigma_c}$, to form a two-dimensional PDF ($\text{BG}_{\text{Combi Bkg w }\Sigma_c}$ in Table II) in $m_{+\pm}$.

The PDFs for combinatorial background with and without genuine Σ_c resonances are validated using studies with MC events and from fits to data within the m_{inv} sidebands of the $m_{\text{inv}}:m_{+\pm}$ planes.

5. non-Σ_c $\bar{B}^0 \rightarrow \Lambda_c^+ \bar{p}\pi^+\pi^-$

Events with $\bar{B}^0 \rightarrow \Lambda_c^+ \bar{p}\pi^+\pi^-$ decays but without signal Σ_c resonances are described by the product of a phenomenological function in $m_{+\pm}$,

$$\begin{aligned}
\text{Y}_{\text{non-}\Sigma_c}&(m_{+\pm}; n, p, q, r; e_{\text{up}}) \\
&= (m_{+\pm} - r) \cdot [m_{+\pm}]^p \cdot (e_{\text{up}} - m_{+\pm})^q, \quad (3)
\end{aligned}$$

and a Gaussian function $\text{X}_{\text{non-}\Sigma_c}(m_{\text{inv}}; \mu, \sigma)$ in m_{inv}. Fits to mixtures of MC samples (denoted as *toy MC mixtures*) are used to validate the combined two-dimensional PDF ($\text{BG}_{\text{non-}\Sigma_c}$ in Table II). This procedure is designed to take into account the fact that $\bar{B}^0 \rightarrow \Lambda_c^+ \bar{p}\pi^+\pi^-$ decays without signal Σ_c resonances can proceed via various other intermediate states besides direct decays into the four-body final state. Since the true composition of $\bar{B}^0 \rightarrow \Lambda_c^+ \bar{p}\pi^+\pi^-$ decays without signal Σ_c resonances is unknown, toy MC sets are created by combining randomly chosen numbers of MC events with completely nonresonant signal decays, signal decays with intermediate non-Σ_c resonances such as N^* or ρ, and signal decays with non-signal Σ_c resonances.
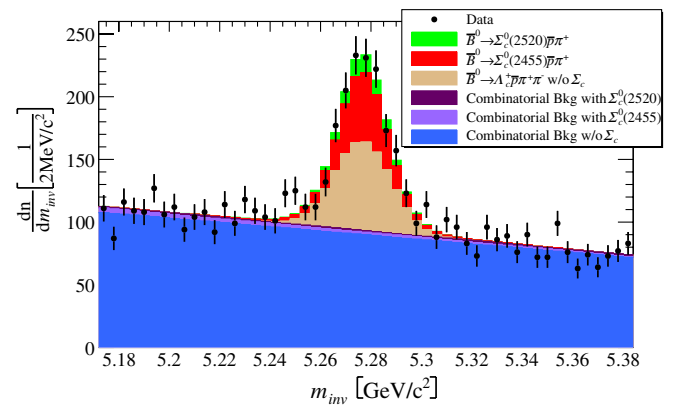

FIG. 5 (color online). Result of the fit to the $m_{\text{inv}}:m_{+-}$ plane projected onto the m_{inv} axis. The data are shown as points with error bars; the fitted signal and background PDFs are overlaid as stacked histograms.
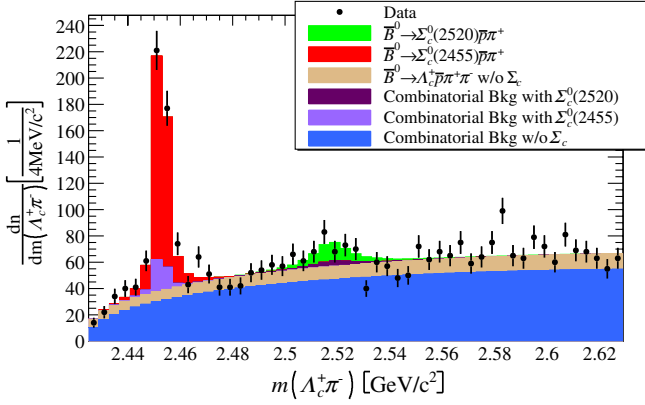
FIG. 6 (color online). Result of the fit to the m_{inv}:m_{+-} plane projected onto the m_{+-} axis. The data are shown as points with error bars; the fitted signal and background PDFs are overlaid as stacked histograms.

In the fits to toy MC samples, a quadratic dependency on $m_{+\pm}$ of the signal-Gaussian width in m_{inv} is observed. This is taken into account by parametrizing the width as $\sigma(m_{+\pm}; a_{\sigma}, b_{\sigma}, c_{\sigma}) = c_{\sigma} \cdot [a_{\sigma} \cdot m_{+\pm}^2 + b_{\sigma} \cdot m_{+\pm} + 1]$. In fits to data, the width parameters are fixed to the values obtained from fits to MC; a systematic uncertainty on the shape is included by varying the parameters within the parameter range obtained from fits to toy MC.

Global PDFs for fits to m_{inv}:m_{++} and to m_{inv}:m_{+-} are formed from sums over the signal and background PDFs as listed in Table II. The global PDFs are validated on toy MC samples of randomly chosen numbers of events from the signal and background classes.

C. Fit results

Maximum likelihood fits to data distributions in the m_{inv}:m_{++} and m_{inv}:m_{+-} planes are performed in the range $m_{\mathrm{inv}} \in [5.17, 5.38]$ GeV/c^2 and $m_{+\pm} \in [2.425, 2.625]$ GeV/c^2, covering the regions of $\Sigma_c(2455)$ and $\Sigma_c(2520)$ resonances.[2]

The fit to m_{inv}:m_{+-} converges with $\chi^2/\mathrm{ndf} = 2807/2697$. Figure 5 shows the projection of the two-dimensional fit onto the m_{inv} axis. The fitted PDFs are shown as stacked histograms and are overlayed with the distribution in data. The projection onto the m_{+-} axis is shown in Fig. 6.

---

[2]Larger $m_{+\pm}$ masses are omitted because of uncertainties on the $\Sigma_c(2800)$ mass values. In a study of the related decay $B^- \to \Lambda_c^+ \bar{p} \pi^-$ [16], a significant difference in the mass is measured for the $\Sigma_c(2800)^0$ resonances with $m(\Sigma_c(2800)^0) = (2.846 \pm 0.008)$ GeV/c^2 compared to the world averaged mass $m(\Sigma_c(2800)^0)_{\mathrm{PDG}} = (2.802^{+0.004}_{-0.007})$ GeV/c^2 [1]. Thus, the histogram PDF approach based on MC simulations is not feasible for $\Sigma_c(2800)$, since the input mass value is necessary for the MC generation.
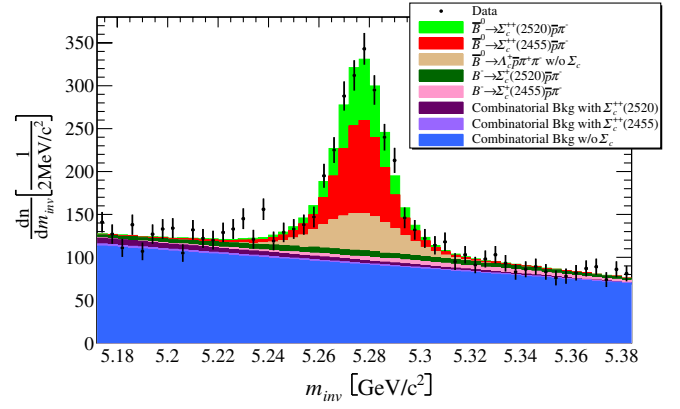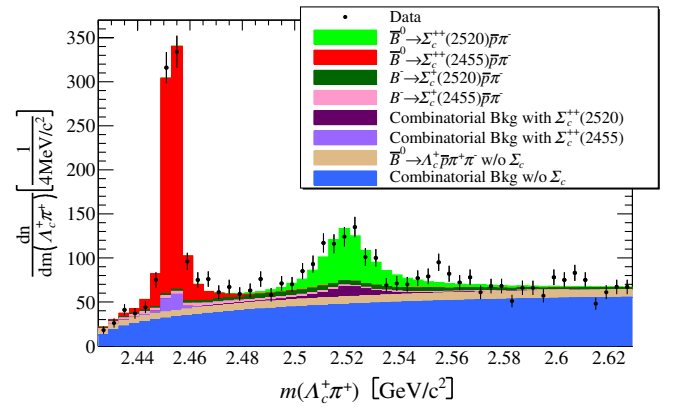

FIG. 7 (color online). Result of the fit to the m_{inv}:m_{++} plane projected onto the m_{inv} axis. The data are shown as points with error bars; the fitted signal and background PDFs are overlaid as stacked histograms.

FIG. 8 (color online). Result of the fit to the m_{inv}:m_{++} plane projected onto the m_{++} axis. The data are shown as points with error bars; the fitted signal and background PDFs are overlaid as stacked histograms.

In the m_{inv}:m_{++} plane, the fit converges with $\chi^2/\mathrm{ndf} = 2592/2695$. The two-dimensional fit results are shown in Fig. 7 for the projection onto m_{inv} and in Fig. 8 for the projection onto m_{++}.

The measured signal yields are given in Table III.

TABLE III. Signal yields without the efficiency correction from the fits to the m_{inv}:$m_{+\pm}$ planes. The uncertainties are statistical.

Mode	Signal yield
$\bar{B}^0 \to \Sigma_c(2455)^0 \bar{p} \pi^+$	347 ± 24
$\bar{B}^0 \to \Sigma_c(2520)^0 \bar{p} \pi^+$	87 ± 27
$\bar{B}^0 \to \Sigma_c(2455)^{++} \bar{p} \pi^-$	723 ± 32
$\bar{B}^0 \to \Sigma_c(2520)^{++} \bar{p} \pi^-$	458 ± 38
$B^- \to \Sigma_c(2455)^+ \bar{p} \pi^-$	164 ± 104
$B^- \to \Sigma_c(2520)^+ \bar{p} \pi^-$	273 ± 133

D. Signal event distributions

The distributions of signal events are extracted using the *sPlot* technique [7] in variables other than the discrimination variables: we perform a fit to the two-dimensional distributions of the signal variables m_{inv} and $m_{+\pm}$ where all shape parameters are fixed, and only the signal yields N_i for each signal and background class i are allowed to vary. Distributions for class i are obtained using per-event weights

$$W_i(m_{\text{inv}}, m_{+\pm}) = \frac{\sum_{j=1}^{N_{\text{total}}} V_{ij} f_j(m_{\text{inv}}, m_{+\pm})}{\sum_{j=1}^{N_{\text{total}}} N_j f_j(m_{\text{inv}}, m_{+\pm})}, \quad (4)$$

where $N_{\text{total}} = \sum N_i$, the N_i and $f_i(m_{\text{inv}}, m_{+\pm})$ are the fitted yield and PDF value for the event in the class i, and

$V_{ij} = \text{Cov}(N_i, N_j)$ is the fit's covariance matrix. We use these weights to generate histograms in Dalitz variables of the $\Sigma_c \bar{p}\pi$ three-body systems. Uncertainties are calculated for *sPlot* histograms with $\sqrt{\sum_i W_i^2}$.

In Fig. 9(a), $\bar{B}^0 \to \Sigma_c(2455)^0 \bar{p}\pi^+$ events are seen to exhibit a sharp enhancement just above the threshold in the $m(\Sigma_c(2455)^0\pi^+)$ distribution; however, there is insufficient information to reliably identify the $\Lambda_c(2595)^+$ or $\Lambda_c(2625)^+$ states. In Fig. 9(b), signal events from $\bar{B}^0 \to \Sigma_c(2455)^0 \bar{p}\pi^+$ accumulate in $m(\Sigma_c(2455)^0\bar{p})$ only for values larger than 3.8 GeV/c^2, clearly ruling out an enhancement at baryon-antibaryon invariant mass
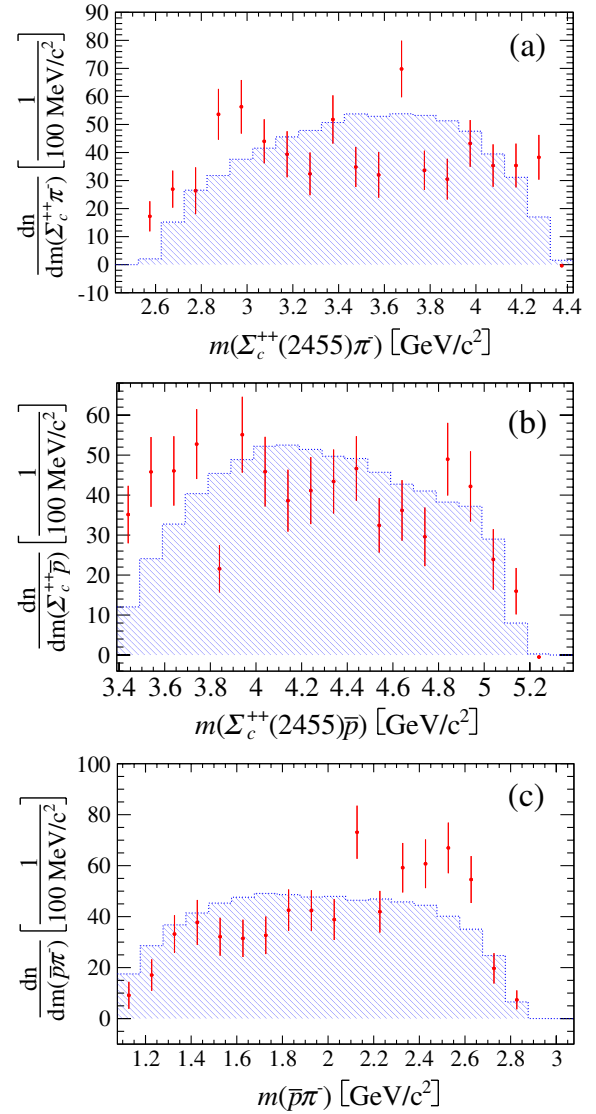

FIG. 9 (color online).   Invariant mass distributions from $\bar{B}^0 \to \Sigma_c(2455)^0 \bar{p}\pi^+$ signal events extracted with the *sPlot* method. Data points are displayed in comparison with the distribution of reconstructed phase-space generated $\bar{B}^0 \to \Sigma_c(2455)^0 \bar{p}\pi^+$ MC events scaled to the same number of entries (shaded histograms).

FIG. 10 (color online).   Invariant mass distributions from $\bar{B}^0 \to \Sigma_c(2455)^{++} \bar{p}\pi^-$ signal events extracted with the *sPlot* method. Data points are displayed in comparison with the distribution of reconstructed phase-space generated $\bar{B}^0 \to \Sigma_c(2455)^{++} \bar{p}\pi^-$ MC events scaled to the same number of entries (shaded histograms).
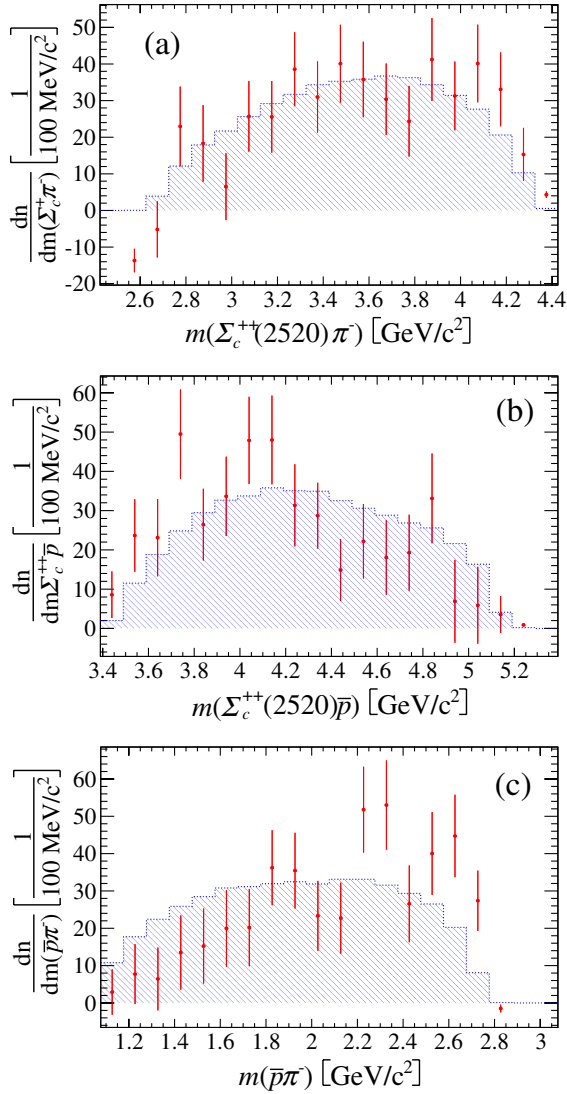
FIG. 11 (color online). Invariant mass distributions from $\bar{B}^0 \to \Sigma_c(2520)^{++}\bar{p}\pi^-$ signal events extracted with the *sPlot* method. Data points are displayed in comparison with the distribution of reconstructed phase-space generated $\bar{B}^0 \to \Sigma_c(2520)^{++}\bar{p}\pi^-$ MC events scaled to the same number of entries (shaded histograms).

threshold, which has been seen in other decays [14,16–19]. Different behavior is observed in Fig. 9(c) where $\bar{B}^0 \to \Sigma_c(2455)^0\bar{p}\pi^+$ events accumulate significantly only for masses $m(\bar{p}\pi^+) < 1.8$ GeV/c^2. Possible sources for this structure could be Δ baryons or N^* nucleon resonances decaying to $\bar{p}\pi^+$. However, due to the overlap of possible broad baryon resonances, we cannot come to a conclusion on specific modes.

The corresponding distributions for $\bar{B}^0 \to \Sigma_c(2455)^{++}\bar{p}\pi^-$ events exhibit different behavior. In the $m(\Sigma_c^{++}\pi^-)$ distribution of Fig. 10(a), no enhancement in the threshold region is visible, while a bump at around 2.9 GeV/c^2 may be due to additional contributions from intermediate $\Lambda_c(2880)^+$ and/or $\Lambda_c(2940)^+$ resonances. In

the $m(\Sigma_c(2455)^{++}\bar{p})$ distribution of Fig. 10(b), events with masses below 3.8 GeV/c^2 contribute prominently, in contrast to the corresponding $m(\Sigma_c(2455)^0\bar{p})$ distribution of Fig. 9(b), making $\bar{B}^0 \to \Sigma_c(2455)^{++}\bar{p}\pi^-$ decays more similar to other baryonic decays [14,16–19]. In Fig. 10(c), events from $\bar{B}^0 \to \Sigma_c(2455)^{++}\bar{p}\pi^-$ are distributed in $m(\bar{p}\pi^-)$ without an obvious structure, unlike events from $\bar{B}^0 \to \Sigma_c(2455)^0\bar{p}\pi^+$ in $m(\bar{p}\pi^+)$ in Fig. 9(c).

The distributions from $\bar{B}^0 \to \Sigma_c(2520)^{++}\bar{p}\pi^-$ in Fig. 11 are similar to the distributions from $\bar{B}^0 \to \Sigma_c(2455)^{++}\bar{p}\pi^-$ events shifted to higher invariant masses.

Because of the relatively small event yield for $\bar{B}^0 \to \Sigma_c(2520)^0\bar{p}\pi^+$ decays, the corresponding *sPlots* are not conclusive, and are therefore not presented.

V. NON-Σ_c $B^0 \to \Lambda_c^+\bar{p}\pi^+\pi^-$ ANALYSIS

The rates of events decaying into the $\bar{B}^0 \to \Lambda_c^+\bar{p}\pi^+\pi^-$ final state without intermediate $\Sigma_c(2455, 2520)^{++}$ or $\Sigma_c(2455, 2520)^0$ resonances are determined in one-dimensional fits to m_{inv}. The non-Σ_c signal yield components measured in the fits to $m_{\text{inv}}:m_{++}$ and $m_{\text{inv}}:m_{+-}$ are not used, since these yields are correlated.

A. Fit strategy and results

The data are divided into two sets: subset m_{inv}^I with $m_{++} < 2.625$ GeV/c^2 and $m_{+-} < 2.625$ GeV/c^2, and subset m_{inv}^{II} with $m_{++} \geq 2.625$ GeV/c^2 and $m_{+-} \geq 2.625$ GeV/c^2. Thus, potential contributions of $B^- \to \Sigma_c(2455, 2520)^+\bar{p}\pi^-$ are confined to the m_{inv}^I subset. In m_{inv}^I, resonant signal events $\bar{B}^0 \to \Sigma_c(2455, 2520)^{++,0}\bar{p}\pi^{\mp}$ are excluded by requiring $m(\Lambda_c^+\pi^{\pm})$ to lie outside $[2.447, 2.461]$ GeV/c^2 and $[2.498, 2.538]$ GeV/c^2.

In the fit of the distribution of m_{inv}^I, background from $B^- \to \Sigma_c(2455)^+\bar{p}\pi^-$ decays is taken into account using a double-Gaussian PDF consisting of two single-Gaussian functions with different means and widths. The shape parameters are fixed to values obtained from signal MC, and the signal yield is fixed to the yield measured in the fit to $m_{\text{inv}}:m_{++}$ (Table III). Similarly, background from $B^- \to \Sigma_c(2520)^+\bar{p}\pi^-$ events is described by a single-Gaussian PDF with fixed shape parameters from MC and the yield fixed to the fitted yield in $m_{\text{inv}}:m_{++}$. Combinatorial background is described with a linear function in m_{inv}. Signal event contributions are described with a double Gaussian with a shared mean; the parameters are allowed to float.

TABLE IV. Signal yields without efficiency correction for decays without intermediate $\Sigma_c(2455, 2520)^{++,0}$ resonances. The first uncertainty is the statistical uncertainty. The second uncertainty for m_{inv}^I denotes the uncertainty on the contribution due to $B^- \to \Sigma_c^+\bar{p}\pi^-$.

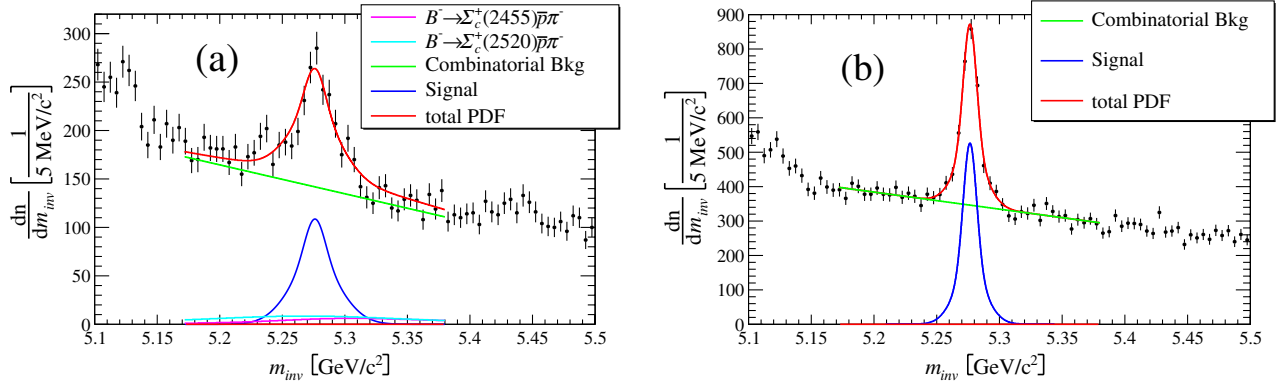| Region	Signal yield
m_{inv}^I	$810 \pm 88 \pm 38$
m_{inv}^{II}	1918 ± 91

FIG. 12 (color online). Fits to m_{inv} distributions of events decaying into the four-body final state $\bar{B}^0 \rightarrow \Lambda_c^+ \bar{p} \pi^+ \pi^-$ without intermediate $\Sigma_c(2455, 2520)^{++,0}$ resonances. In (a) events originate from subset m_{inv}^I excluding the $\Sigma_c(2455, 2520)^{++,0}$ signal regions in m $(\Lambda_c^+ \pi^\pm)$ and taking background from $B^- \rightarrow \Sigma_c(2455, 2520)^+ \bar{p} \pi^-$ into account. In (b) the events originate from subset m_{inv}^{II}.
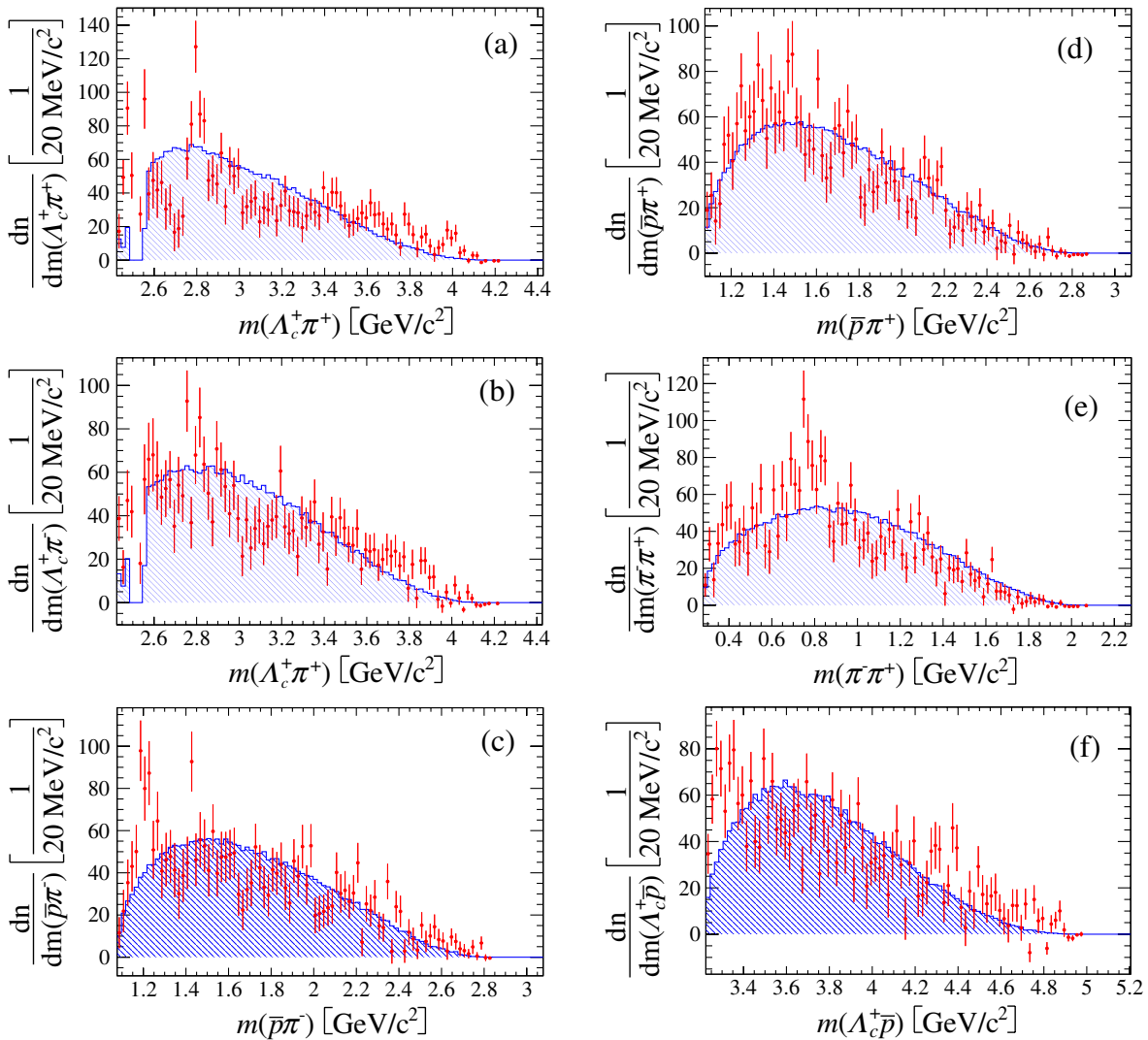
FIG. 13 (color online). Two-body invariant mass distributions for $\bar{B}^0 \rightarrow \Lambda_c^+ \bar{p} \pi^+ \pi^-$ signal events from the combined subsets m_{inv}^I and m_{inv}^{II} extracted with the *sPlot* method. Σ_c resonances are vetoed in the respective invariant masses. Data points are displayed in comparison with the distribution of reconstructed phase-space generated $\bar{B}^0 \rightarrow \Lambda_c^+ \bar{p} \pi^+ \pi^-$ MC events scaled to the same number of entries (shaded histograms).

In the distribution of m_{inv}^{II}, the fit is performed with a first-order polynomial for background and a double Gaussian with shared mean for signal, since no peaking background is expected here.

The fits are shown in Fig. 12 and the yields are given in Table IV.

B. Signal event distributions

Figures 13 and 14 show the combined *sPlots* for non-Σ_c $\bar{B}^0 \to \Lambda_c^+ \bar{p} \pi^+ \pi^-$ events from the fits to m_{inv}^{I} and m_{inv}^{II}.[3] In the $m(\Lambda_c^+ \pi^+)$ distribution of Fig. 13(a), the contribution from intermediate $\Sigma_c(2800)^{++}$ baryons is clearly apparent. The corresponding distribution in $m(\Lambda_c^+ \pi^-)$ is shown in Fig. 13(b); here the isospin related $\Sigma_c(2800)^0$ baryon is less significant. Note that the vetoes on low-mass Σ_c resonances appear as gaps in the distributions. We do not attempt to explicitly measure intermediate states with $\Sigma_c(2800)$ baryons with the present approach. As described in footnote [2], significantly differing masses of $\Sigma_c(2800)$ resonances have been observed in related $B \to \Lambda_c^+ \bar{p} \pi$ decays [16,17], which could originate, amongst other possibilities, from different angular momentum states with similar masses or from contamination due to $B \to D p \bar{p}(n\pi)$ decays. Since the present approach uses *a priori* information on the masses and widths to generate MC-based PDFs, histogram PDFs cannot be applied for states with uncertain masses or widths.

In the distribution of $m(\bar{p}\pi^-)$ in Fig. 13(c), differences are seen compared to the distribution of $m(\bar{p}\pi^+)$ in Fig. 13(d), with events accumulating in $m(\bar{p}\pi^-)$ at values near the lower phase-space boundary, suggesting contributions from decays via $\bar{\Delta}^{--}$. Such a structure does not contribute to $m(\bar{p}\pi^+)$. The $m(\pi^+\pi^-)$ distribution in Fig. 13(e) suggests an intermediate $\rho(770)$ resonance. However, the data are not sufficiently precise to allow a definite conclusion. The $m(\Lambda_c^+ \bar{p})$ distribution in Fig. 13(f) shows some enhancement in the baryon-antibaryon mass near threshold, though less strongly than in other measurements with baryonic final states, e.g., those of Ref. [16]. A conclusive interpretation of the $m(\Lambda_c^+ \bar{p})$ result is difficult, because the MC distribution uses all events in the allowed phase space to avoid a possible bias, averaging over all possible structures. Furthermore, the projections onto the axes of the Dalitz space for the four-final-state-particle system make it difficult to identify reflections from resonances in other invariant masses.

The three-body mass distributions are shown in Fig. 14. Here, we do not observe structures in lower invariant mass ranges that could hint at resonances, e.g., excited Λ_c baryons in $m(\Lambda_c^+ \pi^+ \pi^-)$. The bins near the edges of the

---

[3]The fixed background contributions from $B^- \to \Sigma_c(2455, 2520)^+ \bar{p} \pi^-$ are taken into account in the *sPlot* weight calculations, following the method described in Appendix B of Ref. [7].
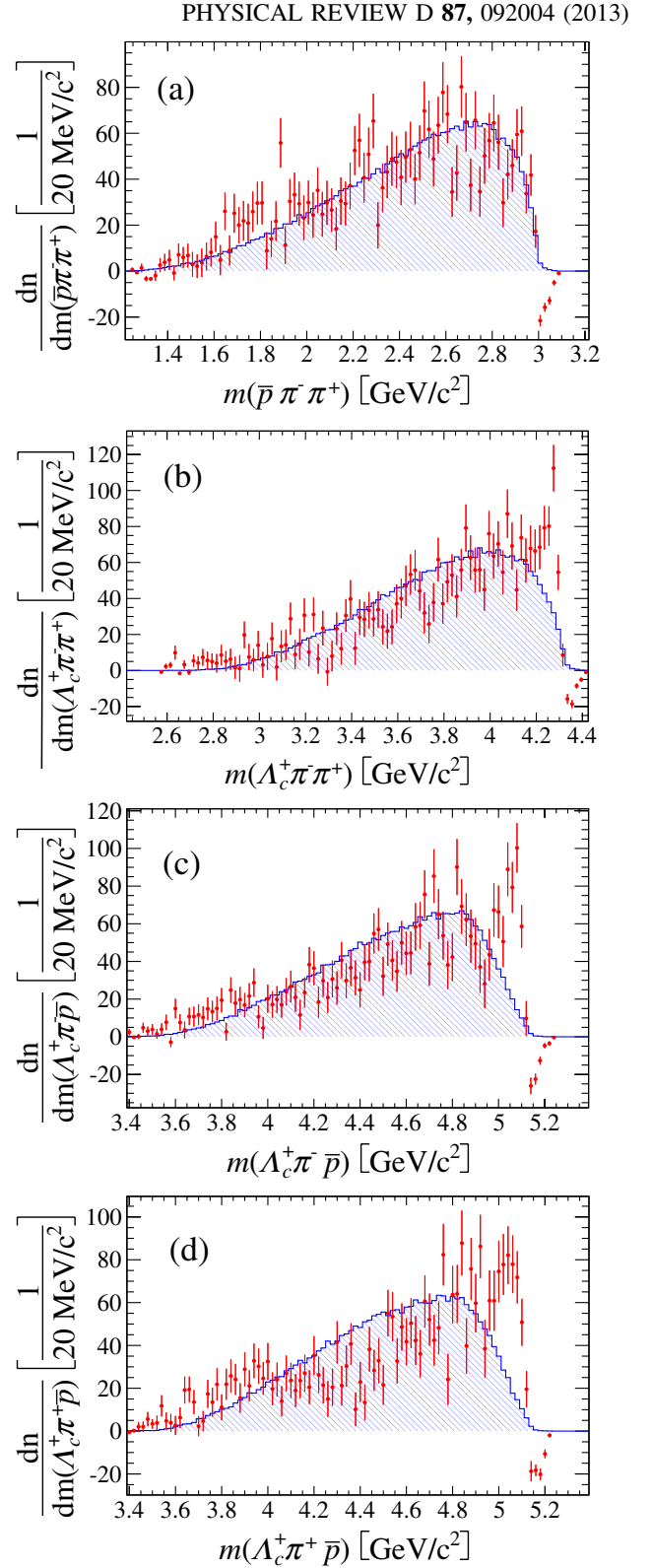

FIG. 14 (color online). Three-body invariant mass distributions for $\bar{B}^0 \to \Lambda_c^+ \bar{p} \pi^+ \pi^-$ signal events from the combined subsets m_{inv}^{I} and m_{inv}^{II} extracted with the *sPlot* method. Data points are displayed in comparison with the distribution of reconstructed phase-space generated $\bar{B}^0 \to \Lambda_c^+ \bar{p} \pi^+ \pi^-$ MC events scaled to the same number of entries (shaded histograms).

distribution are not reproduced correctly by the *sPlot* method, and show artificial undershoots. This is because the *sPlot* technique relies on target variables that are uncorrelated with the discriminating variables. This does not hold for points near the edges of phase space, where there is a dependence on m_{inv}.

VI. EFFICIENCY

The efficiency of the reconstruction is determined separately for each resonant signal mode and for the non-Σ_c signal decays. Since signal MC events are generated uniformly in phase space, the observed decay dynamics are not reproduced. To avoid bias from phase-space-dependent reconstruction efficiencies, the MC samples are iteratively reweighted according to the *sPlot* histograms $\mathcal{N}[m_{a\,b}]_{\mathrm{data}}$ of invariant masses for each signal class from the *B*-meson daughters $a, b, \ldots$. The reweighting is performed iteratively over all two-daughter combinations for each three-body final state and over the three-body combinations for the four-body non-Σ_c final states. Since we do not observe any nontrivial structures in the smooth and moderately varying efficiency distribution before reweighting, we assume that the projections onto the overdetermined Dalitz variables are sufficient for reweighting.

In the initial step $i = 1$, the weight is calculated from the *sPlot* histogram and the signal MC histogram $\mathcal{N}[m_{a\,b}]_{\mathrm{MC}}^{i=1}$ as $w^{i=1}[m_{a\,b}] = \mathcal{N}[m_{a\,b}]_{\mathrm{data}}/\mathcal{N}[m_{a\,b}]_{\mathrm{MC}}^{n=1}$ and applied to each signal MC event. In iteration step n, weights are calculated accordingly from the reweighted signal MC from iteration $n - 1$ for invariant mass $m_{b\,c}$ with $w_{b\,c} = \mathcal{N}[m_{b\,c}]_{\mathrm{data}}/\mathcal{N}[m_{b\,c}]_{\mathrm{MC}}^{n-1}$. In the following, the signal MC events are weighted by $w_{b\,c}$. Since the MC event values processed in step n originate from weighting the MC events in the previous step $n - 1$, the effective weight is $w^n = w^{n-1} \cdot w_{b\,c}$. Negative *sPlot* entries are set to zero to avoid nonphysical weightings.

After each step, a χ^2 fit of the m_{inv} distribution of the reweighted signal MC is performed to obtain the number of reconstructed weighted events. Thus, the reconstruction efficiency is calculated from the number of weighted reconstructed events and the sum of weighted generated events. When the reconstruction efficiencies in the last steps of one cycle through all *B* daughter combinations

TABLE V. Reconstruction efficiencies for each signal event class, after reweighting signal MC events according to *sPlot* distributions.

Mode/region	Reconstruction efficiency
$\bar{B}^0 \to \Sigma_c(2455)^0 \bar{p}\pi^+$	$(16.4 \pm 0.3)\%$
$\bar{B}^0 \to \Sigma_c(2520)^0 \bar{p}\pi^+$	$(16.8 \pm 0.3)\%$
$\bar{B}^0 \to \Sigma_c(2455)^{++} \bar{p}\pi^-$	$(14.5 \pm 0.1)\%$
$\bar{B}^0 \to \Sigma_c(2520)^{++} \bar{p}\pi^-$	$(17.0 \pm 0.2)\%$
$\bar{B}^0 \to \Lambda_c^+ \bar{p}\pi^+ \pi^-_{m_{\mathrm{inv}}^I}$	$(11.6 \pm 0.7)\%$
$\bar{B}^0 \to \Lambda_c^+ \bar{p}\pi^+ \pi^-_{m_{\mathrm{inv}}^{II}}$	$(16.9 \pm 0.1)\%$

are compatible with each other within the uncertainties, we assume that the reconstruction efficiency has converged and we stop the iteration. The reconstruction efficiencies are listed in Table V. The differences between unweighted and weighted efficiencies vary between 2.1% for $\bar{B}^0 \to \Sigma_c(2455)^{++}\bar{p}\pi^-$ and 7.9% for $\bar{B}^0 \to \Sigma_c(2455)^0\bar{p}\pi^+$.

VII. BRANCHING FRACTIONS

The product branching fractions $\mathcal{B}$ are calculated for each signal mode i with

$$\mathcal{B}[\bar{B}^0 \to [\Lambda_c^+\pi^\pm]_{\Sigma_c}\bar{p}\pi^\mp]_i \cdot \mathcal{B}[\Lambda_c^+ \to pK^-\pi^+]$$
$$= \frac{N_{\mathrm{i}}}{N_{B\bar{B}}} \cdot \frac{1}{\varepsilon_i}, \tag{5}$$

where N_{i} is the sum of signal-event numbers (Tables III and IV), ε_i the reconstruction efficiency (Table V), and $N_{B\bar{B}}$ the number $N(\Upsilon(4S))$ of $\Upsilon(4S)$ decays; we assume that $\frac{N(\Upsilon(4S)\to B^0\bar{B}^0)}{N(\Upsilon(4S))} = 0.50$. For an integrated luminosity of $\mathcal{L} = 426$ fb^{-1}, $N_{B\bar{B}} = (467.36 \pm 0.11 \pm 5.14) \times 10^6$, where the uncertainties are statistical and systematic. Σ_c resonances are assumed to decay exclusively into a $\Lambda_c^+\pi$ pair: $\mathcal{B}[\Sigma_c(2455, 2520)^{++,0} \to \Lambda_c^+\pi^\pm] \approx 100\%$ [1]. After accounting for the reconstruction efficiencies, the number of events from the two non-$\Sigma_c(2455, 2520)$ decay measurements are summed and their statistical uncertainties are added in quadrature.

VIII. SYSTEMATIC UNCERTAINTIES

Systematic uncertainties applying to all modes, such as the uncertainty on $N_{B\bar{B}}$, as well as systematic uncertainties specific only to certain modes, are considered. Table VI lists the relative systematic uncertainties $u_x = \frac{\delta N_x}{N_x}$ for each uncertainty x. Systematic uncertainties on the reconstruction efficiency of the six charged final-state tracks are added linearly to obtain a total tracking uncertainty. One of the largest systematic uncertainties originates from the particle identification efficiencies. The uncertainties are evaluated using MC events, with corrections derived from control samples in the data. In addition, MC events are examined without corrections. The relative difference in the particle identification efficiencies with and without the corrections defines the uncertainty. As discussed above, $\bar{B}^0 \to Dp\bar{p}(n\pi)$ decays and decays through charmonia states $\bar{B}^0 \to (c\bar{c})\bar{K}^{*0}[\pi^+\pi^-]$ can yield the same combination of final-state particles as signal events. Based on the known branching fractions [1], a total of at most 4.5 events from these two event classes are expected to satisfy the signal selection criteria. Here, a conservative reconstruction efficiency of $\varepsilon = 0.1\%$ is assumed, overestimating the measured efficiencies in signal MC. The corresponding systematic uncertainty ($B \to D + X$, $c\bar{c} + X$) is set equal to 100% of the corresponding estimated background in line 4 of Table I, for each mode separately.

TABLE VI.   Summary of relative systematic uncertainties $u_i = \frac{\delta N_i}{N_i}$ in [%] for non-Σ_c $\bar{B}^0 \to \Lambda_c^+ \bar{p} \pi^+ \pi^-$, resonant $\bar{B}^0 \to \Sigma_c(2455)\bar{p}\pi^{\pm}$, and resonant $\bar{B}^0 \to \Sigma_c(2520)\bar{p}\pi^{\pm}$ decays. The total systematic uncertainties, added in quadrature, are given in the last row.

Uncertainties u_i [%]	Non-Σ_c	$\Sigma_c(2455)^0$	$\Sigma_c(2455)^{++}$	$\Sigma_c(2520)^0$	$\Sigma_c(2520)^{++}$
$N_{B\bar{B}}$	1.1	1.1	1.1	1.1	1.1
Tracking	1.2	1.2	1.2	1.2	1.2
PID	4.3	4.3	4.3	4.3	4.3
$B \to D + X, c\bar{c} + X$	0.1	0.5	0.5	0.5	0.5
Nonres. shape		0.1	0.1	0.4	0.4
Combi Bkg shape		0.001	0.001	0.7	0.7
Eff. Corr.				0.1	
$B^-(I + II)$	1.8				
$\sqrt{\sum u_i^2}$	4.9	4.6	4.6	4.7	4.7

Only the fits of decays via Σ_c resonances are affected by an uncertainty on the shape of non-Σ_c $B^0 \to \Lambda_c^+ \bar{p} \pi^+ \pi^-$ events in the $m_{\text{inv}}{:}m_{+\pm}$ planes. The parameters on the signal width are varied individually by one standard deviation and the maximum deviation in the event yield is taken as the systematic uncertainty (labeled "nonres.shape" in Table VI). For the shape of combinatorial background, a systematic uncertainty is determined by varying in the PDF the constant describing the end point of the phase space, e_{up}. Fits are repeated with the constant moved from the nominal upper phase-space limit towards the upper end of the fit region in 0.2 GeV/c^2 steps. The maximal deviations in the fitted signal event yields are taken as the systematic uncertainty, labeled "Combi Bkg shape." For histogram PDFs, systematic uncertainties are negligible due to the large size of the input MC data sets. In studies on control variables, we found a good agreement between data and MC-generated events. For deviations of the MC-generated events from data, we applied corrections as described in Sec. IV B 2. An uncertainty, labeled "Eff. Corr.," on the efficiency-calculation weighting is evaluated after completing a cycle through all daughter combinations for each mode. The values converge and are within the statistical uncertainties for all modes after one full cycle, except for $\bar{B}^0 \to \Sigma_c(2520)^0 \bar{p} \pi^+$. For this mode, the efficiencies differ by 1.9%, with a statistical uncertainty of 1.8%, and the difference is taken as an additional systematic uncertainty.

A systematic uncertainty, labeled "$B^-(I + II)$," on the contribution of $B^- \to \Sigma_c(2455, 2520)^+ \bar{p} \pi^-$ events to the non-Σ_c $\bar{B}^0 \to \Lambda_c^+ \bar{p} \pi^+ \pi^-$ yields is calculated by repeating fits to the m_{inv}^I distribution assuming no contribution and overestimating the found contribution by a factor of 2. The maximum deviation of 38 events is included as a systematic uncertainty.

IX. RESULTS

Table VII lists the measured branching fractions for each mode. Because of the large uncertainty on $\mathcal{B}[\Lambda_c^+ \to pK^-\pi^+]$, its systematic uncertainty is given separately.

The uncertainties on the total branching fraction of all $\bar{B}^0 \to \Lambda_c^+ \bar{p} \pi^+ \pi^-_{\text{total}}$ decays are added quadratically when uncorrelated and linearly when correlated.

Because the $\bar{B}^0 \to \Sigma_c(2520)^0 \bar{p} \pi^+$ signal has less than 3 standard deviations significance, we also report a 90% confidence level upper limit for this channel. The upper limit is determined using Bayesian methods, with statistical and systematic uncertainties added in quadrature. We do not include the uncertainty on $\mathcal{B}[\Lambda_c^+ \to pK^-\pi^+]$ in the systematic uncertainty of the upper limit, but factor out the current branching fraction of 0.05 [1]. Assuming a Gaussian distribution, the 90% integral of the physically meaningful region $\mathcal{B} \geq 0$ yields

$$\mathcal{B}[\bar{B}^0 \to \Sigma_c(2520)^0 \bar{p} \pi^+] \cdot \frac{\mathcal{B}[\Lambda_c^+ \to pK^-\pi^+]}{0.05}$$
$$< 3.10 \times 10^{-5} \qquad (6)$$

at the 90% confidence level.

Resonant decays via $\Sigma_c(2455, 2520)$ baryons provide a large contribution to the four-body final state. The ratios of decays via Σ_c resonances in comparison to the largest such mode, $\bar{B}^0 \to \Sigma_c(2455)^{++} \bar{p} \pi^-$, are

$$\frac{\mathcal{B}[\bar{B}^0 \to \Sigma_c(2455)^0 \bar{p} \pi^+]}{\mathcal{B}[\bar{B}^0 \to \Sigma_c(2455)^{++} \bar{p} \pi^-]} = 0.425 \pm 0.036, \qquad (7)$$

$$\frac{\mathcal{B}[\bar{B}^0 \to \Sigma_c(2520)^{++} \bar{p} \pi^-]}{\mathcal{B}[\bar{B}^0 \to \Sigma_c(2455)^{++} \bar{p} \pi^-]} = 0.541 \pm 0.052, \qquad (8)$$

while the fraction of all decays that proceed via the $\Sigma_c(2455)^+ \bar{p} \pi^-$ mode is

$$\frac{\mathcal{B}[\bar{B}^0 \to \Sigma_c(2455)^{++} \bar{p} \pi^-]}{\mathcal{B}[\bar{B}^0 \to \Lambda_c^+ \bar{p} \pi^+ \pi^-]_{\text{total}}} = 0.174 \pm 0.047. \qquad (9)$$

In these three results, systematic uncertainties common to the numerator and denominator cancel, and only the systematic uncertainties specific to each mode are added in quadrature. The three-body intermediate states have comparable branching fractions to the nonresonant three-body decays $B \to \Lambda_c^+ \bar{p} \pi$ [8,9,16,17,20].

TABLE VII. Branching fractions of the resonant decays $\bar{B}^0 \to \Sigma_c(2455, 2520)^{++,0} \bar{p}\pi^{\mp}$ and non-$\Sigma_c(2455, 2520)$ decays $\bar{B}^0 \to \Lambda_c^+ \bar{p}\pi^+\pi^-$ where the first uncertainty is statistical, the second systematic, and the third due to the uncertainty on the $\mathcal{B}[\Lambda_c^+ \to pK^-\pi^+]$ branching fraction.

Mode/region	$\mathcal{B}[\bar{B}^0] \cdot \mathcal{B}[\Lambda_c^+ \to pK^-\pi^+]$ $[10^{-6}]$	$\mathcal{B}[\bar{B}^0]$ $[10^{-5}]$
$\bar{B}^0 \to \Sigma_c(2455)^0 \bar{p}\pi^+$	$(4.5 \pm 0.3 \pm 0.2)$	$(9.1 \pm 0.7 \pm 0.4 \pm 2.4)$
$\bar{B}^0 \to \Sigma_c(2455)^{++} \bar{p}\pi^-$	$(10.7 \pm 0.5 \pm 0.5)$	$(21.3 \pm 1.0 \pm 1.0 \pm 5.5)$
$\bar{B}^0 \to \Sigma_c(2520)^0 \bar{p}\pi^+$	$(1.1 \pm 0.4 \pm 0.1)$	$(2.2 \pm 0.7 \pm 0.1 \pm 0.6)$
$\bar{B}^0 \to \Sigma_c(2520)^{++} \bar{p}\pi^-$	$(5.8 \pm 0.5 \pm 0.3)$	$(11.5 \pm 1.0 \pm 0.5 \pm 3.0)$
$\bar{B}^0 \to \Lambda_c^+ \bar{p}\pi^+\pi^-_{\text{non-}\Sigma_c}$	$(39.2 \pm 2.2 \pm 1.9)$	$(79 \pm 4 \pm 4 \pm 20)$
$\bar{B}^0 \to \Lambda_c^+ \bar{p}\pi^+\pi^-_{\text{total}}$	$(61.3 \pm 2.4 \pm 3.7)$	$(123 \pm 5 \pm 7 \pm 32)$

The measured branching fractions are in good agreement with previous measurements from Belle [9].

X. SUMMARY

We observe the decay $\bar{B}^0 \to \Lambda_c^+ \bar{p}\pi^+\pi^-$, study the intermediate decays via $\Sigma_c(2455)^{++}$, $\Sigma_c(2520)^{++}$, $\Sigma_c(2455)^0$, and $\Sigma_c(2520)^0$ resonances, and measure their branching fractions (Table VII). Yields for events decaying to $\bar{B}^0 \to \Lambda_c^+ \bar{p}\pi^+\pi^-$ without intermediate $\Sigma_c(2455, 2520)^{++,0}$ resonances are obtained from one-dimensional fits in m_{inv}, taking information from fits to $m_{\text{inv}}{:}m_{+\pm}$ into account. For all decay modes, we show the *sPlot* distributions of the signal, and we observe significant differences between decays into $\Sigma_c^{++}\bar{p}\pi^-$ and $\Sigma_c^0\bar{p}\pi^+$ final states.

ACKNOWLEDGMENTS

[1] K. Nakamura *et al.* (Particle Data Group), J. Phys. G **37,** 075021 (2010).

[2] M. Savage and M. Wise, Nucl. Phys. **B326,** 15 (1989).

[3] W.-S. Hou and A. Soni, Phys. Rev. Lett. **86,** 4247 (2001).

[4] H.-Y. Cheng and K.-C. Yang, Phys. Rev. D **65,** 054028 (2002).

[5] H.-Y. Cheng and K.-C. Yang, Phys. Rev. D **67,** 034008 (2003).

[6] M. Suzuki, J. Phys. G **34,** 283 (2007).

[7] M. Pivk and F. Le Diberder, Nucl. Instrum. Methods Phys. Res., Sect. A **555,** 356 (2005).

[8] S. A. Dytman *et al.* (CLEO Collaboration), Phys. Rev. D **66,** 091101 (2002).

[9] K. S. Park *et al.* (Belle Collaboration), Phys. Rev. D **75,** 011101 (2007).

[10] B. Aubert *et al.* (*BABAR* Collaboration), Nucl. Instrum. Methods Phys. Res., Sect. A **479,** 1 (2002).

[11] D. Lange, Nucl. Instrum. Methods Phys. Res., Sect. A **462,** 152 (2001).

[12] T. Sjöstrand, Comput. Phys. Commun. **82,** 74 (1994).

[13] S. Agostinelli *et al.*, Nucl. Instrum. Methods Phys. Res., Sect. A **506,** 250 (2003).

[14] P. del Amo Sanchez *et al.* (*BABAR* Collaboration), Phys. Rev. D **85,** 092017 (2012).

[15] B. Aubert *et al.* (*BABAR* Collaboration), Phys. Rev. D **72,** 052006 (2005).

[16] B. Aubert *et al.* (*BABAR* Collaboration), Phys. Rev. D **78,** 112003 (2008).

[17] B. Aubert *et al.* (*BABAR* Collaboration), Phys. Rev. D **82,** 031102 (2010).

[18] B. Aubert *et al.* (*BABAR* Collaboration), Phys. Rev. D **79,** 112009 (2009).

[19] B. Aubert *et al.* (*BABAR* Collaboration), Phys. Rev. D **76,** 092006 (2007).

[20] J. P. Lees *et al.* (*BABAR* Collaboration), Phys. Rev. D **86,** 091102 (2012).